Spring 2017

Investigation of Low Cost Substrate Approaches for III-V Solar Cells

Marlene Lydia Lichty
Old Dominion University

INVESTIGATION OF LOW COST SUBSTRATE APPROACHES FOR III-V SOLAR CELLS

by

Marlene Lydia Lichty
B.S. May 2014, Christopher Newport University

A Thesis Submitted to the Faculty of
Old Dominion University in Partial Fulfillment of the
Requirements for the Degree of

MASTER OF SCIENCE

ELECTRICAL AND COMPUTER ENGINEERING

OLD DOMINION UNIVERSITY
May 2017

Approved by:

Christopher G. Bailey (Director)

Sylvain X. Marsillac (Member)

Gon Namkoong (Member)

ABSTRACT

INVESTIGATION OF LOW COST SUBSTRATES APPROACHES FOR III-V SOLAR CELLS

Marlene Lydia Lichty
Old Dominion University, 2017
Director: Dr. Christopher G. Bailey

With the need for cleaner energy sources, which can displace fossil fuel, the solar cell industry is of particular interest due to the abundancy of the Sun. Silicon currently dominates terrestrial applications, but efficiency improvements have saturated. III-V based solar cells have reported the highest efficiencies, however, high costs due to substrates and fabrication processes have limited these devices to specialty applications, such as space. In order to reduce the cost associated with fabricating III-V semiconductor substrate material, two different approaches were taken in this work with a particular focus on making III-Vs more applicable outside of specialty applications, including InP, InAsnd Ge. Typical material characterization techniques were used to analyze the samples and processes studied in this thesis. The first process examined was the direct epitaxial growth of III-V materials by MOCVD on cheaper substrates. More specifically, the direct growth of InP and InAs on metal foils. A growth time study and surface coverage analysis was performed for the growth of InP. A characterization study was then conducted on the second process, the aluminum- induced crystallization of germanium to determine the effects this process had on the surface. Crystalline InP, InAs and Ge were successfully characterized in this work, and show promise for use in cheaper III-V alternatives to terrestrial energy solutions.

ACKNOWLEDGEMENTS

I would like to first thank my committee chair, Dr. Christopher Bailey, for his support, patience and guidance. Thank you for being so patient and flexible with my schedule and for challenging me throughout this process. I am extremely grateful for all the knowledge I have gained from working on your research team. I would also like to express appreciation to Professor Sylvain Marsillac and Professor Gon Namkoong for serving on my thesis committee. I want to thank Dr. Marsillic for providing me with the opportunity of shadowing his graduate students. I am extremely grateful for that opportunity and for exposing me to a solar cell lab and clean room. I also would like to thank Dr. Namkoong for introducing me to the subject and informing me about the possibilities and opportunities at ODU involving solar cell research. His class was the first solar cell class I had ever taken. I appreciate all that you taught me about the fundamentals and principles of solar cells. Additionally, I would like to thank Dr. Wei Cao, Applied Research Center, for taking the time and having patience in training me on the characterization tools, in addition to sharing his knowledge. This research was supported by the National Science Foundation (NSF)'s Solar Engineering Academic Program (SoLEAP). I am extremely grateful for all the opportunities and knowledge this program has provided.

TABLE OF CONTENTS

Page

LIST OF TABLES vii

LIST OF FIGURES viii

Chapter

1. INTRODUCTION 1
   - 1.1 THE NEED FOR SOLAR ENERGY 1
   - 1.2 III-V SOLAR CELL HISTORY 2
   - 1.3 COST LIMITATIONS OF III-VS 5
   - 1.4 THESIS OBJECTIVES 6

2. EXPERIMENTAL METHODS EMPLOYED 8
   - 2.1 METALORGANIC CHEMICAL VAPOR DEPOSITION 8
   - 2.2 ALUMINUM- INDUCED CRYSTALLIZATION 11
   - 2.3 X-RAY DIFFRACTION (XRD) 12
   - 2.4 PHOTOLUMINESCENCE (PL) 14
   - 2.5 SCANNING ELECTRON MICROSCOPY (SEM) 15
   - 2.6 ENERGY DISPERSIVE X-RAY SPECTROSCOPY (EDS) 17
   - 2.7 ATOMIC FORCE MICROSCOPY (AFM) 18
   - 2.8 IMAGEJ SOFTWARE 20

3. DIRECT EPITAXY OF INDIUM PHOSPHIDE ON MOLYBDENUM FOIL 22
   - 3.1 SAMPLE P-1 RESULTS AND DISCUSSION 23
   - 3.2 SAMPLE P-2 RESULTS AND DISCUSSION 29
   - 3.3 SAMPLE P-3 RESULTS AND DISCUSSION 33
   - 3.4 GROWTH TIME COMPARISON FOR SAMPLES P-1, P-2 AND P-3 38

4. DIRECT EPITAXIAL GROWTH OF INDIUM ARSENIC ON MOLYBDENUM FOIL 42
   - 4.1 SAMPLE A-1 RESULTS AND DISCUSSION 43

5. CHARACTERIZATION STUDY OF ALUMINUM-INDUCED CRYSTALLIZATION OF GERMANIUM 50
   - 5.1 SAMPLE AL-1 RESULTS AND DISCUSSION 51
   - 5.2 SAMPLE AL-2 RESULTS AND DISCUSSION 56
   - 5.3 SAMPLE AL-3 RESULTS AND DISCUSSION 57
   - 5.4 SAMPLE AL-4 RESULTS AND DISCUSSION 58
   - 5.5 SAMPLE AL-5 RESULTS AND DISCUSSION 62
   - 5.6 COMPARISON AND CONCLUSIONS OF AIC-GE PROCESS 67

6. CONCLUSIONS 69
   - 6.1 SUMMARY 69
   - 6.2 FUTURE WORKS 71

BIBLIOGRAPHY 72

VITA 76

LIST OF TABLES

Table Page

1.1 Comparison of Material Parameters for Si, GaAs, and InP 3

1.2 Cost Comparison of Common Substrates 6

3.1 Sample List for Direct Epitaxy of InP on Mo Foil by MOCVD 23

3.2 Atom Percentage of Sample P-1 27

3.3 Atom Percentage of Specific Location Analysis for Sample P-2 33

3.4 Atom Percentage of Specific Location Analysis for Sample P-3 37

3.5 Comparison of Sample P-1, P-2, and P-3 41

4.1 Atomic Percentages for Specific Point Measurement for Sample A-1 47

5.1 AIC-Ge Sample List and Parameters 51

5.2 Atom Percentages for Specific Location Analysis for Sample Al-4 62

5.3 Atom Percentages of Specific Point Measurement for Sample Al-5 67

LIST OF FIGURES

Figure Page

2.1 Left: MOCVD Machine, Right: Horizontal Reaction Chamber Located within the MOCVD 10

2.2 Schematic diagram of the aluminum induced crystallization process. (a) Layers applied, (b) Layer structure before annealing, (c) During annealing process, and (d) Layer structure after annealing 12

2.3 XRD results for an InAs sample with labelled known peaks and molybdenum peaks 14

2.4 PL of two InP samples compared to InP wafer 15

2.5 SEM image of InP sample grown by MOCVD on Mo foil showing islanding 17

2.6 Left: SEM image of InP MOCVD grown sample, Right: EDS mapping results for Indium. . 18

2.7 AFM tool used to analyze samples in this research 19

2.8 AFM 3-D results from the Nanoscope software showing surface roughness details 19

2.9 Left: SEM image of InAs sample showing islanding, Right: ImageJ results with islands identified and outlined. 21

3.1 XRD of Sample P-1 with labelled peaks for InP and Mo 24

3.2 SEM Images of Sample P-1 surface features and island structures 25

3.3 EDS spectrum of sample P-1 with labelled elemental energies and intensities 26

3.4 EDS mapping of Sample P-1: (a) In, (b) As, (c) P, (d) Mo, (e) SEM Image 27

3.5 PL results for Sample P-1 compared to InP substrate 28

3.6 XRD of Sample P-2 with labelled peaks for InP (18) and Mo (3) 30

3.7 SEM images of Sample P-2 surface features and coverage, left: magnification of 330x and right: magnification 1,500x 30

3.8 EDS Spectrum of Sample P-2 with labelled energy peaks 31

3.9 EDS Mapping Results for Sample P-2 32

3.10 EDS Point and Shoot for Sample P-2 with locations of the points taken for analysis 33

Figure Page

3.11 XRD results for Sample P-3 with labelled peaks for InP and Mo 34

3.12 SEM Images of Sample P-3..... 35

3.13 EDS Spectrum of Sample P-3 with labelled energy peaks 35

3.14 EDS Mapping of Sample P-3 36

3.15 EDS Point and Shoot locations for Sample P-3 37

3.16 XRD results comparison for Sample P-2 and P-3 with labelled crystal planes 38

3.17 PL results comparison for Samples P-2 and P-3 39

3.18 SEM Comparison for Samples P-1, P-2, and P-3 for magnifications of 330x and 1,500x .. 40

4.1 XRD Results of Sample A-1 with labelled peaks 44

4.2 SEM images of Sample A-1 44

4.3 EDS Spectrum for Sample A-1 with labelled peak intensities 45

4.4 EDS mapping of Sample A-1: (a) In (b) As (c) Mo (d) SEM 46

4.5 Corresponding SEM Image for EDS P&S of Sample A-1 showing the location of the points used for further elemental analysis 47

4.6 AFM results for Sample A-1 showing 3-d surface roughness with quantitative results 48

4.7 Left image: SEM, Right Image: Island density and surface coverage of Sample A-1 49

5.1 Sample structure of aluminum-induced crystallization of germanium on silicon wafer with corresponding layer thicknesses 51

5.2 SEM results left image: 1,600x and right image: 23,000x zoomed in on light and dark feature 52

5.3 Additional SEM images at magnifications of 750x and 7,500x 53

5.4 EDS results for a dark spot on Sample Al-1 with corresponding SEM 54

5.5 EDS results of light spot located above the surface with SEM image 55

5.6 Cross-sectional SEM of sample Al-1 56

Figure Page

5.7 SEM of a crater on Sample Al-2 surface 56

5.8 Cross-sectional SEM of sample Al-2 57

5.9 SEM images for Sample Al-3, (a) magnification x1,000, (b) dark spots, (c) light spots, (d) zoomed in dark spot 58

5.10 SEM of the surface features on Sample Al-4. 59

5.11 Right: SEM used for EDS analysis and Left: SEM showing where the zoomed feature is located 60

5.12 EDS results for Sample Al-4 with corresponding SEM 61

5.13 EDS point and shoot of Sample Al-4 with the corresponding SEM including the point locations analyzed 62

5.14 SEM results of Sample Al-5 showing cracks on the surface 63

5.15 EDS Results for Sample Al-5 for the crack and dark region located on the surface 64

5.16 EDS results for Sample Al-5 for the interesting raised feature located on the surface..... 65

5.17 Additional SEM results of surface features found on Sample Al-5 66

5.18 EDS Point and Shoot on the additional surface features found on Sample Al-5 67

CHAPTER 1

INTRODUCTION

1.1 The Need for Solar Energy

With the rise in carbon dioxide emission and depletion of fossil fuels, the need for a cleaner reliable energy source is ever increasing. The photovoltaic (PV) industry has the potential to vastly change the way energy is consumed and produced. The solar cell industry is increasingly growing and advancing. This renewable energy continues to gain more attention in terms of being a direct way of producing cleaner energy [1, 2]. Photovoltaics can help alleviate issues associated with fossil fuels because it is a clean energy source that can reduce carbon emissions and has immense potential due to the vast availability of the sun's energy [2].

Photovoltaics work by converting the sun's energy in the form of photons into electricity. More specifically, these photons emitted from the sun hit the solar cell and free electrons, because these solar cells are composed of a semiconductor material treated to form a p-n junction, meaning positive on one side and negative on the other. When electrical conductors are placed on top and bottom of a solar cell, these freed electrons can be captured to create an electrical circuit producing electricity [3]. The semiconductor material has a specific bandgap associated with it, the energy required for an electron to move from the valance band to the conduction band. Photons can only free electrons in the semiconductor if their energy is either equal to or larger than this bandgap, meaning a specific semiconductor material can only absorb the part of sun's spectrum above the bandgap value. Photons with energy less than the bandgap are not absorbed, and in sense are wasted [3]. To maximum the absorption of photons, multiple cells with different bandgap energies are stacked in descending order with the largest bandgap material on top, forming a multijunction solar cell. These solar cells can achieve higher efficiency because more of the sun's spectrum is absorbed and converted into electricity. Efficiency is defined as the solar radiation percentage converted to electricity [2].

Silicon has dominated the PV industry. In 2010, approximately 80% of solar cell production was based on silicon materials. Silicon's abundant availability, cheaper cost, and ability to maintain reliability lasting for 20 to 25 years has led to this silicon driven industry [2]. However,

silicon has an indirect bandgap and a low absorption coefficient, which is a major downfall for use in optoelectronic applications, such as with multijunction solar cells [4]. Additionally, silicon is limited when it comes to efficiency and lattice matched opportunities, whereas III-V solar cell materials have great potential for multijunction applications and clearly surpass Si in efficiency [2].

1.2 III-V Solar Cell History

III-V based solar cells have come extremely far since the first photovoltaic device was developed, which reached only a 6% efficiency back in 1954 [5]. This efficiency keep climbing, and by the late 1970s, IBM TJ Watson demonstrated that a III-V based GaAs solar cell could achieve a 22% efficiency [5]. However, silicon dominated the industry because of its lower cost and availability, which contributed to its fast climb in efficiencies reaching, for monocrystalline, a 25% efficiency and, for polycrystalline, 20.4% [5]. There are a number of reasons why researchers continued to push for improving III-V qualities despite their initial lack in efficiency and quality due to their extreme potential. GaAs and InP are two very important III-V materials. Table 1.1 shows this potential of these two important binaries with a comparison of material parameters for silicon, GaAs and InP. The values in this table were received from the following sources [5-11]. Today, photovoltaics made from III-V materials have consistently achieved the highest power conversion efficiencies, passing 45% and are the clear front runner [6].

Table 1.1 Comparison of Material Parameters for Si, GaAs, and InP

Material Parameters	Si (E_g = 1.12eV)	GaAs (E_g = 1.43eV)	InP (E_g = 1.34eV)
Δ Bandgap (eV) from optimal SQ value (1.34eV)	0.22 eV	0.09 eV	0.00 eV
Absorption Coefficient @ bandgap (cm^{-1})	$<10^2$	$\sim10^4$	$\sim10^4$
Direct Bandgap	No	Yes	Yes
Electron Mobility ($cm^2/V*s$) (300k)	700	4600	4000
SRV (cm/s)	$\sim10^2$-$8x10^4$	$\sim10^6$	$\sim10^3$
Radiation Tolerant	No	Extremely	Yes
Available for Multijunction	Depends	Yes	Yes
Toxic / Rare Materials	No / No	Yes / Yes	Yes / Yes

In terms of having an ideal bandgap based on the Shockley Queisser value of 1.34 eV, the difference for silicon is 0.22 eV, whereas GaAs is only slightly larger by 0.09eV. InP matches with the ideal bandgap of 1.34eV. Additionally, InP and GaAs both have direct bandgaps and higher absorption coefficients than Si. Silicon's indirect bandgap contributes to its lower absorption coefficient. The lower SRV of InP makes it ideal for polycrystalline applications. Another advantage of GaAs and InP over Si is there radiation tolerance, which is imperative for space applications. Additionally, III-V materials, such as the two listed in the table, are better suited for multijunction applications because of the variety of lattice matched materials. Silicon has some advantages in terms of abundancy in material and not being a toxic material. GaAs and InP both have toxic components, arsenic and phosphorous, as well as rare materials, including arsenic and indium. However, material systems are developed enough where toxicity issues can be mitigated [5-8].

GaAs is one III-V material that is particularly important because it has an ideal and direct bandgap, which allows for stronger absorption of the solar spectrum reaching 1.4ev [5]. In addition to GaAs, InP also has an ideal bandgap, but a lower surface recombination velocity (SRV) than GaAs, making InP better suited for polycrystalline materials [6]. To achieve high efficient III-V polycrystalline solar cells, InP is better suited because of its low SRV of approximately 10^3cm s^{-1} to decrease the effects of increased grain boundaries [6]. This is a major advantage compared to silicon. In addition, Si requires a much larger layer of active material, close to 50μm, but GaAs and InP only need an active layer of a few μm [5]. III-Vs are not only the leader in terms of power conversion efficiency, but especially for radiation hardness, making them ideal for space applications [5]. III-V materials are the best option for multijunction applications because of their wide range of bandgaps and lattice constants, in addition to their variety of material and optical properties [4]. MOCVD has been studied extensively in the past for polycrystalline GaAs, but studies concerning growth techniques for polycrystalline InP and InAs are limited.

In addition to GaAs and InP, InAs is also an important III-V binary material. InAs has an electron mobility value around $20x10^3$ $cm^2/V*s$ at room temperature, which is another advantage over GaAs whose mobility is several times smaller [8]. The low bandgap, 0.36eV, of InAs makes it very useful in photodetectors, especially for the range of 1-3μm, in addition to optoelectronic devices in the long wavelength range [8] [12]. InAs can also be used as the material for the electron quantum well in the electronic devices with the following structure: InAs/GaSb/AlSb [12]. The combination of InP and InAs makes a very useful III-V ternary compound, InAsP. This ternary has a direct bandgap throughout and spans a bandgap range of 0.35eV to 1.35eV, in addition to its high electron mobilities [12, 13].

III-V based materials have many advantages, including the highest efficiencies, ideal bandgap, multijunction ability, and direct bandgap. These materials are ideal for space applications, but have the potential to vastly improve commercial uses of solar cells if a few improvements were made. If III-V based materials were expanded beyond specialty applications, they could significantly impact the energy field in terms of how energy is produced. The improvements needed to make these materials more applicable can be mitigated with a few adjustments, while still having high-quality III-V based materials.

1.3 Cost Limitations of III-Vs

Despite III-V photovoltaics having the highest efficiencies, they are limited to specialized applications, such as space devices and high concentration uses, due to the high cell cost [11]. Even though III-Vs are expensive, space applications depend on III-V high efficiency solar cells because they have a higher "specific power", meaning power per weight, whereas for terrestrial uses the costs are measured as $/watt. These high costs of III-Vs are attributed to the scarcity of the materials and the expensive substrates [4]. Molecular beam epitaxy (MBE) and metal organic chemical vapor deposition (MOCVD) are used for growing III-V photovoltaic materials because these tools are capable of growing high quality III-V crystals. The machines are also tunability in terms of bandgap and altering the binary stoichiometry to achieve ternaries and even quaternaries to from multiple junctions, while maintaining lattice constant [5]. The III-V industry is focused on improving the quality of thin film III-V solar cells [5]. Typically, the substrate makes up 80-90% of the total cost of fabricating a solar cell [11]. Finding ways to reduce substrate costs is essential in expanding III-V solar applications. There are different strategies being investigated to reduce the costs associated with fabricating III-V solar cells, such as wafer reuse, epitaxial lift off (ELO), and metal foils [11]. However, ELO can result in unwanted drop in efficiency if these devices were chemically-polished [5]. Refinishing of the substrate surface can improve efficiency lost, but not completely [5]. Using alternative substrates, such as metal foils, may result in polycrystalline growth, but provide a cheap and flexible option with a high thermal stability [6].

Germanium (Ge) is another important substrate for use as the bottom cell in triple junction III-V multijunction applications because it aligns closely with GaAs's lattice constant and has a low bandgap [5, 14]. However, the thick monocrystalline substrate is expensive and makes up most of the solar cell cost for III-V's [14]. Ge and GaAs substrates can cost around $150 per wafer [11]. Currently, the cost for a GaAs 2-inch single crystalline undoped wafers ranges from $140-$160, whereas for InAs wafer the costs are approximately, $599-$620 [15]. Utilizing lower cost techniques for III-V materials results in polycrystalline formation. Therefore, obtaining large grain size is necessary in making III-V solar cells more practical outside of specialty applications [14]. Large grain size can be achieved with the recrystallization process of Ge with a capping layer of aluminum, but can be prone to cracking, dewetting and peeling. Reducing stress

during the recrystallization of Ge is important in making this a viable option for reducing these issues. The aluminum-induced crystallization (AIC) process can be used to alleviate stress on the germanium layer during the process of forming a polycrystalline substrate in order to reduce the cost associated with typically Ge substrates [14].

Table 1.2 shows the cost comparison for various substrates, including Si, GaAs, Ge, InP, and InAs. GaAs, Ge and InP substrates are more expensive when compared to Si and InAs is even more expensive. Silicon beats out the other substrates in terms of cost for not only substrate cost, but for the growth processes and fabrication of these materials. Using cheaper substrates, such as foils or thin films, to grow thin films of III-V will lead to polycrystalline formation, resulting in constraints with recombination due to the increase in grain boundaries, but can decrease the expense associated with III-Vs [6]. Using III-V materials with a low SRV can reduce the effects of the increase in grain boundaries and can lead to high-quality polycrystalline solar cells. The focus of this thesis is on decreasing substrate costs and improving crystal quality by growing thin film III-V materials on cheaper substrates, in addition to investigating methods for fabricating cheaper substrates commonly used for III-V multijunctions. The information in the table received from the following sources [6, 11, 15] .

Table 1.2 Cost Comparison for Common Substrates

Costs	Si/Ge	GaAs	InP	InAs
Substrate	$/$$	$$$$	$$$$	$$$$$
Growth Process	$/$$	$$$$	$$$$	$$$$

1.4 Thesis Objectives

Monumental strides have been made in the solar industry with efficiency values over the past 50 years, but there is still potential for even bigger impacts from III-V solar cells, if the costs are reduced. Higher efficiencies can be achieved, but there is still a need for low-cost high efficient solar cells to further expand and launch the photovoltaic industry ahead. III-V based solar cell materials with cheap substrates are well suited to accomplish this task of expanding terrestrial applications. This thesis characterizes materials to address issues associated with low-cost cheap substrates for III-V materials and applications.

The objective of this thesis is to analyze and report on two processes for achieving lower cost III-V substrate materials through a characterization study of the results, in order to make III-V based solar cells more practical outside of specialty applications. Materials investigated include InP, InAs, and Ge. Chapter 2 starts with a discussion on why the two growth processes, MOCVD and AIC, were chosen and used, as well as the advantages and disadvantages associated with each one. The various characterization techniques that were used to analyze the samples and the principles behind these tools used are then discussed. Chapter 3 discusses the results from doing a growth time study of directly growing InP on a cheaper substrate, Mo foil, by MOCVD to improve surface coverage. XRD and PL results closely aligned with the accepted values for InP, and surface coverage improved. Chapter 4 discusses the results of utilizing that same direct growth process, but for InAs on Mo foil. Lattice constant and bandgap results are reported that are in line with accepted values for InAs and surface roughness was investigated. Chapter 5 reports on the characterization study from investigating a different approach to achieving cheaper substrates by aluminum induced crystallization of germanium, since Ge is a very important substrate for III-V multijunction applications. This characterization study showed the effects that stress can have on the layer transfer of aluminum and germanium.

CHAPTER 2

EXPERIMENTAL METHODS EMPLOYED

The experimental techniques used in this research are important for fabricating high-quality polycrystalline material. Material quality is essential for high-efficiency polycrystalline solar cells. The characterization tools are extremely useful in analyzing surface details and crystal quality. The results obtained from these characterization techniques will be used to predict how III-V solar cells made from PX material might perform. In this work, many of the resources at Old Dominion University are exploited for the characterization studies. At Old Dominion University, there is access to a variety of characterization machines. The physics and operation of these tools will be explained in this chapter. Characterization methods, including x-ray diffraction (XRD), photoluminescence (PL), scanning electron microscopy (SEM), energy dispersive x-ray spectroscopy (EDS), and atomic force microscopy (AFM) are used to further determine the composition of the samples fabricated and to quantitatively and qualitatively evaluate the samples studied in this work. More specifically, a JOEL SEM tool equipped with an EDS detector was used to determine elemental analysis and an x-ray diffractometer was used to investigate the structural lattice details. PL was used to investigate the optical properties, the bandgap and material quality. AFM was used to determine the roughness of the surface. The "ImageJ" software package by the National Institutes of Health (NIH) was used to determine the surface coverage of the samples.

2.1 METALORGANIC CHEMICAL VAPOR DEPOSITION

There are two epitaxial growth techniques for III-V materials, which include molecular beam epitaxy (MBE) and metalorganic chemical vapor deposition (MOCVD), each with its own set of advantages and disadvantages. MBE is a growth technique that is performed under ultrahigh vacuum (UHV). This process involves a heated substrate in which the evaporation of elemental sources occurs, and at these low pressures, the mean free path is long, resulting in very precise layer growth and high uniformity, especially over a large area. However, MBE is expensive due

to the use of UHV and has limits regarding commercial uses due to its low growth rate, resulting in a low throughput [16, 17]. Additionally, MBE can have difficulties with growing P-containing alloys because phosphorous will collect in the vacuum pumps [16]. This requires further shut down time for cleaning, limiting throughput even more.

The growth process technique used in Chapter 3 was the direct epitaxial growth by MOCVD. It has the most flexibility, a high purity level, a simple reactor design, and uniform characteristics. This growth technique involves the use of expensive reactants and hazardous precursors, but is favorable for the growth of III/V semiconductor materials, because it has a higher throughput making it more applicable for commercial usages [16]. MOCVD along with other crystal growth processes are very complex, which will be further discussed later on.

The understanding of the MOCVD growth process has increased vastly over the past, especially since the 1990s with the incorporation of in situ monitoring during the growth process, which has also improved control over growth process variables, including gas flow rates and temperatures [16]. Unlike with MBE, reflection high-energy diffraction (RHEED) used to monitor the surface conditions in MBE cannot be used in MOCVD because of the electron beam sources. Photons are being used for probes in MOCVD because they can penetrate the gases near the surface without modifying the chemical composition, whereas RHEED cannot [16, 17]. The key processes involved that affect growth with this technique include: thermodynamics, mass and heat transport, physical surface processes, chemical reactions, and subsurface processes. This can be simplified into two main components involved with crystal growth, thermodynamics and kinetic principles [16].

For the MOCVD growth process used here, a substrate is placed on a heated graphite susceptor located inside the main quartz tube. In terms of III-V semiconductor material, gases for the group III alkyls and group V hydrides flow into a quartz tube and are carried by a hydrogen (H_2) carrier gas. The substrate is heated from the stand contributing to the catalytic effect that takes place when the gases come near the surface causing the decomposition or “cracking” of the precursor gases, leading to the adsorption of individual III and V constituents onto the substrate surface in an organized arrangement, forming crystal growth [17]. MOCVD is relatively simple in design compared to other growth techniques and with the ability to quickly switch on and off gases, which can produce superlattices, multi-quantum wells and heterostructures [17]. Growth with MOCVD can produce multilayers of a few atomic layer thicknesses. However, the

MOCVD process has some disadvantages associated with it, including the use of poisonous gases and difficulties with in situ characterization, which has been improving over the years [17].

The MOCVD machine used in this research is seen in Fig. 2.1. The right image shows the inside of the MOCVD, which shows the horizontal structure of the reaction chamber. The slight angle of the susceptor in the horizontal design as opposed to the vertical design, creates a more uniform deposition and increases the depletion of reactants from the incoming gas flow [17]. The susceptor is located inside the reaction chamber underneath the white radiofrequency (RF) coil, which is used for induction. The susceptor is located near the gas flow inlet, which is an important aspect for the reaction to maximize growth from the gases. Carrier gases, including H_2 or N_2, limit pre-reaction and allow for the mixing of gases to take place, which in turn improves the growth quality of the material [17].

Fig. 2.1: Left: MOCVD Machine, Right: Horizontal reaction chamber located within the MOCVD machine

Molybdenum was chosen as the metal foil substrate because of its low solubility with Indium, Phosphorous and Arsenic, in addition to its lower cost and flexibility characteristics [6]. Molybdenum foils were polished and cleaned with a concentrated cleaning solution of Micro-90 in an ultrasonic bath to prevent any organic or impurity contamination before the growth process occurred. Epitaxial material was then grown for Indium Phosphide using Trimethyl Indium and

Phosphine and for Indium Arsenic using Triethyl Indium and Arsine (AsH_3). A growth temperature of 620°C and a pressure of 150 Torr was used for all samples involving the MOCVD growth process, discussed in Chapters 3 and 4. Chapter 3 goes into more detail about growth thickness and growth time as it pertains to the samples studied here.

2.2 ALUMINUM-INDUCED CRYSTALLIZATION

The main portion of III-V cost is attributed to the expensive semiconductor substrates of monocrystalline structure. By improving polycrystalline materials with large grain sizes can contribute to low-cost III-V photovoltaics. Germanium is of particular importance due to is usefulness in III-V multijunction applications. Its low bandgap makes it ideal for GaAs-lattice matched architectures. Ge, however, can be expensive in terms of substrate cost [14]. Another method for achieving lower stress and low cost polycrystalline substrates is with the aluminum-induced crystallization (AIC) process of germanium. Thermal annealing of the Al/Ge dual stack forces the aluminum through the germanium leading to the recrystallization of germanium as a precipitate of the layer transfer [14]. This has been widely studied for various applications, such as how the thickness of Ge/Al affected the AIC of Ge on glass substrates and how stacking sequence with bilayers can affect the crystallization of Ge [18-20].

For AIC, Aluminum is deposited between the substrate and germanium layer. Annealing the sample causes the aluminum layer to diffuse through the germanium layer by layer transfer, migrating to the surface. This process of annealing decreases the stress on the crystallization of the germanium layer, which was formed during deposition. After the layer transfer, the aluminum layer can be etched off leaving a polycrystalline germanium layer [14]. A schematic of the layer structure and process steps is seen in Fig. 2.2 (a-d). Fig. 2.2(a) and (b) show the initial structure of the al-induced setup with amorphous germanium as the top layer above aluminum. Fig. 2.2 (c) depicts the process during annealing, showing the aluminum diffusing into the germanium layer. Fig. 2.2 (d) shows the structure after annealing, with aluminum layer now as the top layer with a polycrystalline germanium layer underneath.

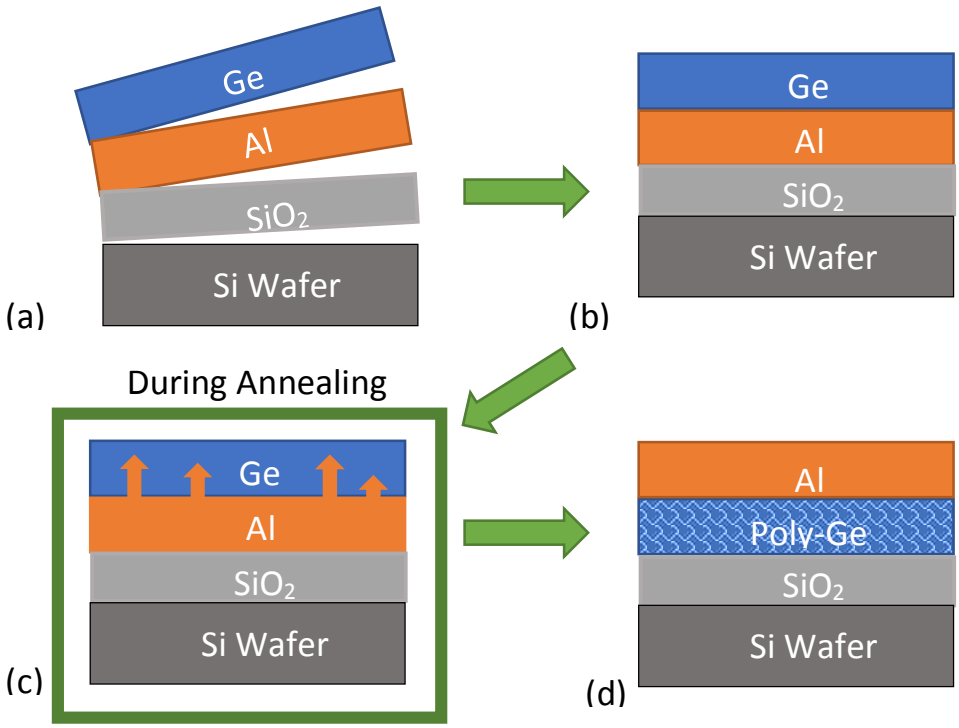

FIG. 2.2. Schematic diagram of the aluminum induced crystallization process. (a) Layers applied, (b) Layer structure before annealing, (c) During annealing process, and (d) Layer structure after annealing

Chapter 5 discusses the results from work that has been done on aluminum crystallization of germanium on a silicon wafer. While the work involving the growth and annealing of the AIC-Ge samples was done off campus, growth characterization methods were performed on campus. This work involved using a Bruce Diffusion Furnace to thermally grow a layer of SiO_2, 500nm, on a 2in silicon wafer, which was n-type with a 111 orientation. The Aluminum deposited layer thickness was 50nm, while germanium layer range was 200-600 nm. The thermal evaporator used to deposit these layers was a Kurt J. Lesker PVD 75. An Aixtron Metal-Organic Vapor Phase Epitaxy reactor (MOVPE) was used to anneal the samples with set point temperatures of 480° C and 500° C and ramp rates of 1 °C/s and 0.1 °C/s [14].

2.3 X-RAY DIFFRACTION (XRD)

XRD was used in this study to investigate the structural details and to calculate lattice constant. A Miniflex II Benchtop X-Ray Diffractometer (Rigaku), which is a scintillation

counter, was used for XRD measurements in this thesis. X-ray Powder Diffraction (XRD) utilizes a powder component in order to diffract monochromatic x-rays, meaning the alpha radiation's strong Kα component emitted from an x-ray tube, operating above the potential of the target materials k-excitation. Powder can mean actual powder bonded together or a polycrystalline sample [21]. The latter was the form used for this research since the work involved polycrystalline (PX) material. This method is particularly effective for measuring polycrystalline material because of its non-destructive measures and does not require special sample preparation [21].

XRD is useful for investigating structural details, such as the spacing between crystal planes, of a material. X-rays, in general, are converted by detectors into electric current surges. Electronic components process these surges or pulses for a period of time, which is proportional to the incoming x-ray beam intensity [21]. A diffractometer is used for examining crystalline materials by measuring the scattered or diffracted x-rays [21]. For this research, the main focus was on x-ray diffraction utilizing the kinematic diffraction theory for calculating lattice constants of thin films. By utilizing this theory, Bragg's law can be used to calculate lattice constant throughout this research and the calculation methods will be discussed in Chapter 3. An example XRD result is seen in Fig. 2.3 with the labelled peaks that aligned with known polycrystalline InAs peaks. In this example, twelve known peaks are identified and the intensity gives further insight on crystalline structure. This example also shows how the XRD tool can detect the substrate material, in this case, molybdenum.

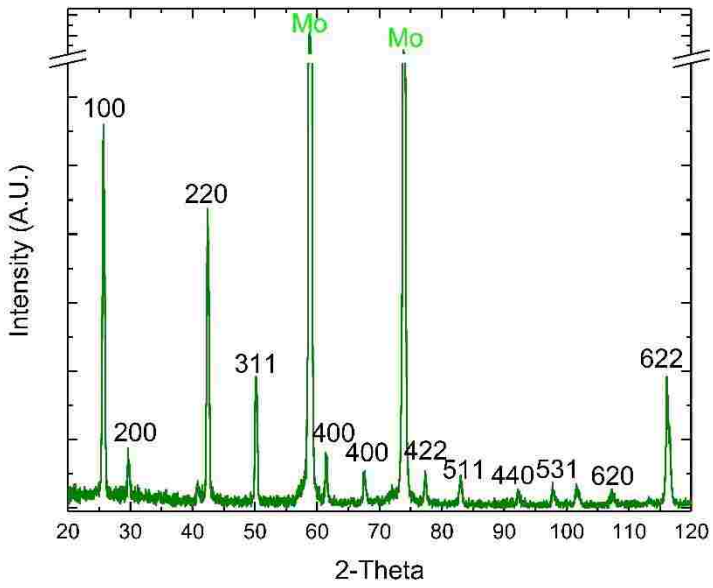

FIG. 2.3. XRD results for an InAs sample with labelled known peaks and molybdenum peaks.

2.4 PHOTOLUMINESCENCE (PL)

PL spectroscopy is a very common method used to determine optical material quality of semiconductors, in addition to material lifetime and semiconductor impurity levels or defects [22, 23]. PL was used in this study to investigate the optical quality, more specifically bandgap. The full-width half-maximum (FWHM) gives useful information about crystal quality. One particularly useful result from the PL spectra is bandgap because band-to-band radiative recombination of electron-hole pairs is indicative of energy bandgap, particularly, helpful in verifying optically-active material band structure. A disadvantage to PL is its extreme sensitive to electric fields, but this process is non-destructive and it can be useful for examining materials in terms of their electronic properties, more specifically, in excited states [23]. This process involves the absorption of photons exciting an electron to the conduction band, also known as photoexcitation, which when it recombines, emits radiation [23].

Photoluminescence was used in one study for temperature dependence study of intensity, position and shape of the band structure to gain information regarding defects, as well as using PL to aid in identifying these defects [22]. PL was also used in another study to determine bandgap and comparison to an InP single crystal results [6]. An example of photoluminescence for MOCVD growth in this research is seen in Fig. 2.4. PL was used in this research to determine

bandgap, FWHM details, and comparison to a single crystalline InP substrate. The settings used in all the measurements shown in this work included a Si detector, a laser with a power of 500mW and light wavelength of 532nm.

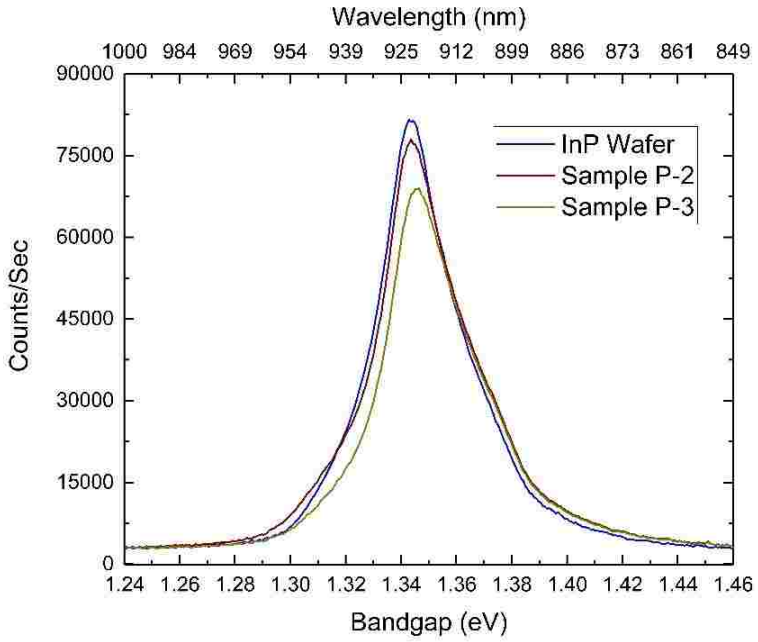

FIG. 2.4. PL of two InP samples compared to InP wafer.

2.5 SCANNING ELECTRON MICROSCOPY (SEM)

SEM is a characterization technique used to analysis surface features and morphology. It can be used in a wide range of applications from chemistry to biology and in this research for material science. The SEM utilizes an electron beam of high energy instead of a light source, which has significantly improved the resolution and capabilities of the microscope. The addition of electromagnetic lenses helps focus the electrons' short wavelengths. As a result, the SEM is capable of imaging in the high-resolution range, which for modern SEM tools can be as low as 1nm. The electron beam coming in contact with the sample being studied creates two types of signals that are important for analyzing the morphology. These signals are backscattering electrons (BSEs), which involves the elastic scattering process, and secondary electrons (SEs), which involves the inelastic scattering process, in addition to characteristic x-rays, which is useful for chemical analysis of the sample [24].

With elastic scattering, the incident electron is deflected when it comes in contact with the specimen's electrons in the outer shell or the atomic nucleus. The electrons are considered backscattered when the change in direction from the incident electron is larger than 90°. This process creates an important imaging signal. An electron within the sample can be set into motion by a large transfer of energy and is called a secondary electron, which can then become scattered or leave the specimen. This process is known as inelastic scattering, which can also produce an image of the specimen surface [24]. In this research, secondary electron imaging is the primary imaging mode used.

The SEM is an average of the first few layers of depth into the sample. The interaction volume of the electron beam of scattered electrons is dependent on accelerating volume and is often referred to as a "tear drop" shape. Secondary electrons have low energy and are useful for analyzing the first few layers of the sample of thickness ranging from 50-500 angstroms, which makes them especially sensitive to surface features. The processing of secondary electrons for imaging is the more common approach for SEM and has a better resolution associated with this process, because the production of SEs is small in comparison to BSEs and X-rays. The BSE can travel the next furthest into the specimen. The X-rays penetrate the deepest into the sample and are extremely useful for determining chemical composition [24].

A negative charge build-up can occur because of the high-energy electrons bombarding the sample if a sample is not electrically conductive. Coatings of electrically conductive material, such as gold or platinum, are often sputtered on the surface of insulating samples prone to negative charge build up. The coating provides an escape for the electrical field. These coatings can obscure surface features if applied to thick [24]. There are some limitations associated with SEM. First, a sample may become damaged because of the bombardment of electrons on the surface, in addition to radiation damage, resulting in artifacts. Another concern is contamination, which is more common at high magnifications and accelerating voltages in the low range. The main cause of contamination is the adsorbed organic molecules, which originate from the atmosphere and vacuum parts, bonding in the electron irradiation [24].

An example of an SEM image is seen in Fig. 2.5 of an indium phosphide polycrystalline sample on Molybdenum foil, which takes advantage of the secondary electron image capabilities of the SEM. SEM imaging was used to further investigate surface coverage and crystal

appearance throughout this research, along with cross-sectional SEM to determine layer thickness.

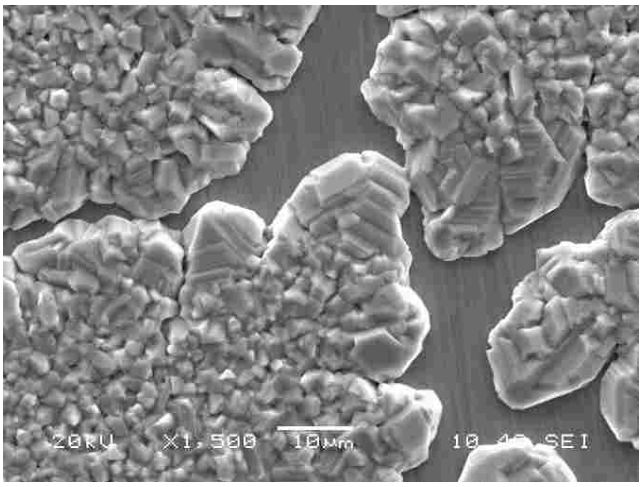

FIG. 2.5. SEM image of InP sample grown by MOCVD on Mo foil showing islanding.

2.6 ENERGY DISPERSIVE X-RAY SPECTROSCOPY (EDS)

EDS was used in this research to identify elements present, map out a surface's elemental composition, and even analyze a particular point on the sample called the "point-and-shoot" method. The SEM tool in this research is equipped EDS capabilities. EDS involves capturing and analyzing the characteristic x-rays signals emitted from the sample being bombarded with electrons, as mentioned in the previous section. When an incoming electron collides with and displaces an electron located in the inner-shell, an electron in the outer-shell will drop and replace the missing inner shell electron in order to rebalance the charge, in turn ionizing the atom [24]. Emission of an x-ray photon occurs in order to return to the ground state [24]. Each shell of the atom has certain energy amounts associated with them.

The x-ray radiation produced from the release of the photon of an atom can be used to identify elemental composition because each atom has distinct energy values associated with each of its shells [24]. An SEM equipped with EDS functions can be used to produce x-ray images, which records the location of a certain characteristic x-ray, to map out the elemental distribution [24]. An example of an EDS map with the corresponding SEM image is seen in Fig. 2.6. This example of EDS mapping is of indium, which is detected only on the islands, meaning the islands are composed of Indium. EDS Mapping is extremely useful for determining spatial

orientation of elemental composition and can also help identify if contamination is present in a sample and where it is located.

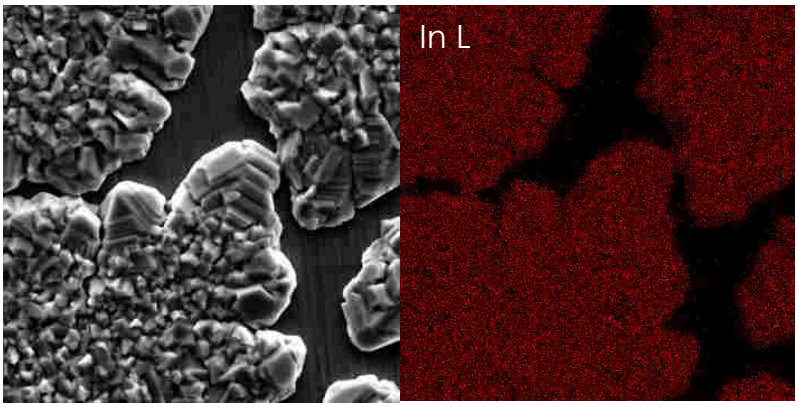

FIG. 2.6. Left: SEM image of InP MOCVD grown sample, Right: EDS mapping results for Indium.

2.7 ATOMIC FORCE MICROSCOPY (AFM)

In this research, tapping-mode AFM was utilized to analyze surface roughness. This method oscillates the cantilever and the tip comes in contact with the surface for a short amount of time [25]. Atomic force microscopy is a technique used to further analyze surface features. AFM produces an image from the interaction between a sharp-small tip, which is attached by a cantilever with the surface of a sample, more specifically by measuring the cantilever deflection once it comes near the surface. Interatomic repulsive forces are used on a short scale AFM signal [25]. AFM is useful for determining Root Mean Square (RMS) value, which is the integral average roughness value, useful for determining thickness. Fig. 2.7 shows the AFM tool used in this research to analyze samples. The sample stage is located on the bottom on the round disk. The AFM tip head is located right above the sample stage. The photodetector adjustment knobs are located above the tip holder on the left, and the laser adjustment knobs are located on top. The camera is placed to the left of the image tip. The vacuum switch, which controls holding the sample in place, is located on the main portion of the tool on the upper right.

FIG. 2.7. AFM tool used to analyze samples in this research.

The tool's native 'Nanoscope' software was used to analyze the results. An example of the AFM results from the Nanoscope software is seen in Fig. 2.8. This technique was used for analyzing surface roughness and shows the three-dimensional capabilities of the software. The color range associated with the height differences in the sample is seen to the right of the image. In the upper left, the AFM values from the sample, including RMS, are seen. The upper right data lists information about the scan size, rate and scale.

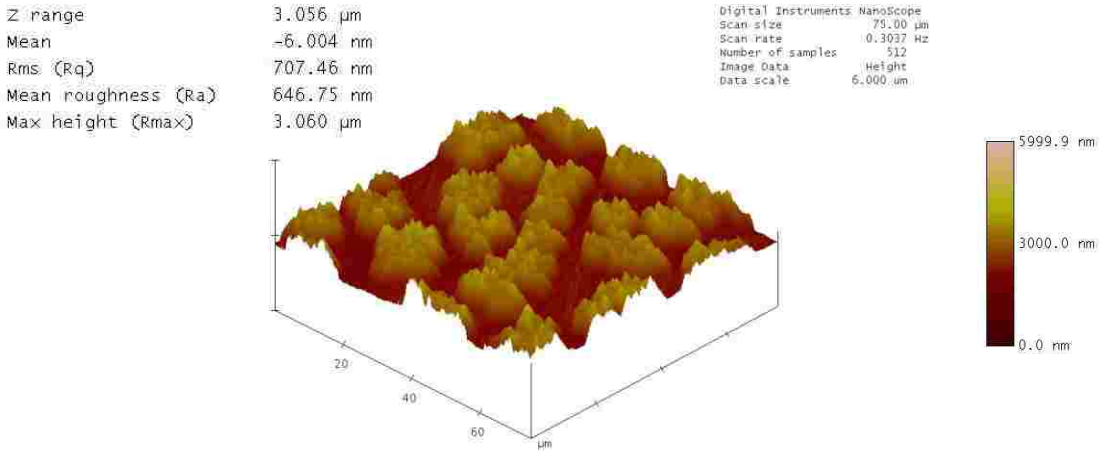

FIG. 2.8. AFM 3-D results from the Nanoscope software showing surface roughness details.

2.8 IMAGEJ SOFTWARE

ImageJ can analyze an SEM image and be used to identify the number of islands, as well as the percentage of the surface they cover. ImageJ is capable of providing additional information concerning surface features. ImageJ first converts an image to grayscale. The threshold tool function is used to distinguish between the background and the objects under investigation. The threshold function allows the image to be adjusted in order to further differentiate between the background and features. This feature separates the particles of interests from the background [26]. The "Analyze Particles" function can count the number of particles above the threshold, represented by the black particles. The threshold value is found after the image has been converted to grayscale, represented by 8 or 16 bits. The threshold value is the intensity value that represents the standard between particles of interest and the background, everything above this value is colored white and everything below is colored black [26]. The ImageJ software utilizes an algorithm analysis method to add up all the black particles. The shape and size of these particles counted can be set and adjusted. Another feature is the "fill in holes" function, which will count everything inside the outline as part of the particle by using the edge and a close loop function. This is useful in improving accuracy of the analysis. This information can be particularly useful for determining surface coverage.

ImageJ is widely used in multiple disciplines. In one study, ImageJ was used for biology purposes to count the number of cells in a specific location [26]. In another study, ImageJ was used to identify and determine the spacing of crystal planes by analyzing the transmission electron microscopy (TEM) images [27]. ImageJ was used to produce surface plots of the samples crystal planes in order to determine the spacing between planes [27]. In the research for this paper, ImageJ was utilized for spatial coverage analysis. An example result of using ImageJ to identify the islands and surface coverage is seen in Fig. 2.9. ImageJ software was able to identify the number of islands and outline the islands in order to give information concerning spatial coverage of the sample.

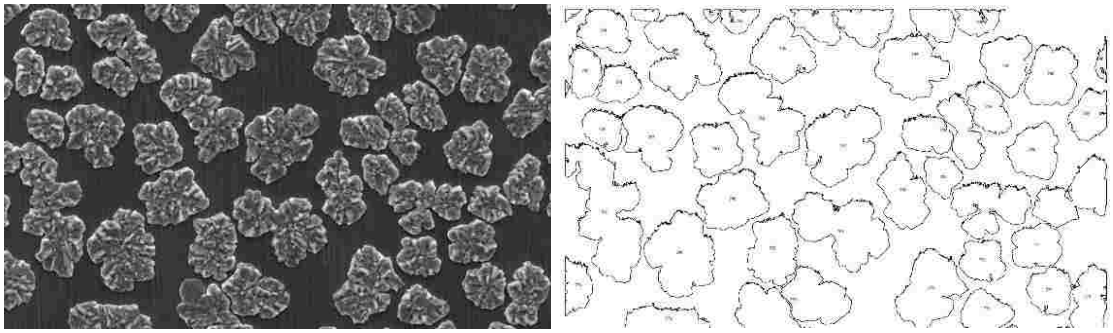

FIG. 2.9 Left: SEM image of InAs sample showing islanding, Right: ImageJ results with islands identified and outlined.

These characterization tools were used extensively throughout this research to analyze the samples fabricated from the two growth techniques, MOCVD and AIC. The use of the AFM technique was limited due to the machine's limitations with the surface roughness. These variety of characterization techniques were extremely helpful in providing insight on material quality and surface details. Each of these techniques offered a key piece of useful information in determining the effectiveness of the growth process.

CHAPTER 3

DIRECT EPITAXIAL GROWTH OF INDIUM PHOSPHIDE ON MOLYBDENUM FOIL

As previously discussed, III-V photovoltaic materials have consistently benchmarked world record power conversion efficiencies [6, 10]. These materials are highly suitable for solar cell designs involving multijunctions because of III-V's wide material properties and optical range [4]. Costs associated with these materials is often high due to the materials, substrates, and fabrication processes [4]. By directly growing these materials on metal foils, substrate costs can be reduced. InP is of particular interest due to its low surface recombination velocity (SRC), leading to efficient polycrystalline material, ideal bandgap, high electron motilities and a direct bandgap [6, 10, 28]. This chapter focuses on increasing growth time of the direct growth of InP on Mo foils to improve surface coverage using an MOCVD. It should be noted that thickness will be reported in growth time instead of nm or μm because the growth process is not explicitly 2D layers.

In this research, islanding or Volmer-Weber growth was observed because the bond between InP atoms was stronger than the bond of these atoms to the surface of the foil, which could be attributed to the large lattice mismatch between InP and the Mo foil [29, 30]. The Volmer Weber growth mode has isolated 3-D islands, at first, formed by nucleation sites, which continue to grow until they impinge on one another, eventually coalescing to form a polycrystalline thin film of a continuous medium [31]. This growth 3-D growth process was present because of the lattive mismatch between the metal foils and growth material of InP. The initial nucleation sites play an important role in material quality in terms of grain size and structure [32]. This growth mode has some drawbacks associated with it, including a discontinuous medium resulting from the islands [31]. The focus of this chapter is on increasing growth time in an effort to allow the islands to coalesce in order to approach a continuous thin film of polycrystalline InP to eventually be able to grow and fabricate a solar cell.

An investigation took place on how growth time affected the surface coverage of the direct growth process of indium phosphide on molybdenum foil using an MOCVD tool, in addition to

determining if crystal structure was present and the alloy composition present. Three samples were fabricated at growth times that varied by 1x, 2x, and 3x, consisting of 49 minutes, 98 minutes and 147 minutes, respectively. Table 3.1 shows the sample names and corresponding growth times. A growth temperature of 620 ° C was used for all samples, as well as a pressure of 150 torr. This temperature was chosen because large grain sizes were seen with temperatures above 545°C in another research study [6]. This pressure is a typical pressure recipe for III-V growth. This chapter shows the results from the characterrization study done on each sample, including XRD, SEM, EDS, and PL techniques. A surface coverage analysis and comparison was also conducted for these samples using ImageJ to determine which growth time had the best spatial coverage.

Table 3.1 Sample List for Direct Epitaxy of InP on Mo Foil by MOCVD

Sample Name	Growth Times
P-1	49 minutes
P-2	98 minutes
P-3	147 minutes

3.1 SAMPLE P-1 RESULTS AND DISCUSSION

This section discusses the results from various characterization techniques, including XRD, SEM, EDS, and PL that were used to analyze Sample P-1 . This sample was the direct epitaxy of InP on Mo foil for a growth time of 49 minutes. XRD was conducted first to determine if InP was present in the sample. XRD was used to identify the Miller indices and to determine the lattice constant. Fig. 3.1 shows this data plotted with the Miller indices of the identified lattices planes for InP. The intensities of the InP peaks are not as strong as the Mo peaks. There are only four peaks identified, which could be caused by the lack of coverage of the sample. There were no significant peak intensities past 80 degrees. There are two Molybdenum peaks detected from the foil beneath the epitaxy layer and are labelled in the plot. The blue vertical dash lines represent where the known InP peaks should to be located [33]. As seen in Fig. 3.1, the peaks for Sample P-1 are offset slightly from known InP peaks, indicating a potential contamination. Using Bragg's law, equation (1), to calculate lattice constant from the XRD data, a lattice

constant of 5.94 Å was obtained, which shows that there is some form of contamination in the alloy, since the published lattice constant for InP is 5.86 Å. Due to the lattice constant being larger than the known lattice constant of InP, arsenic contamination was suspected to have occurred from the reactor. The reactor had some arsenic residue that could have easily been desorbed from the sides of the machine when it is heated, because arsenic had been previously used in the reactor. Vegard's Law, equation (2), was used to determine the ternary composition, resulting in $InAs_{0.39}P_{0.61}$ [21]. Further characterizations were conducted to determine if in fact that contamination was arsenic.

$$\mathrm{d} = \frac{\lambda}{2}\frac{1}{sin(\theta)} \qquad (1)$$

$$a_{A_{(1-x)}B_x} = (1-x)a_A + xa_B \qquad (2)$$

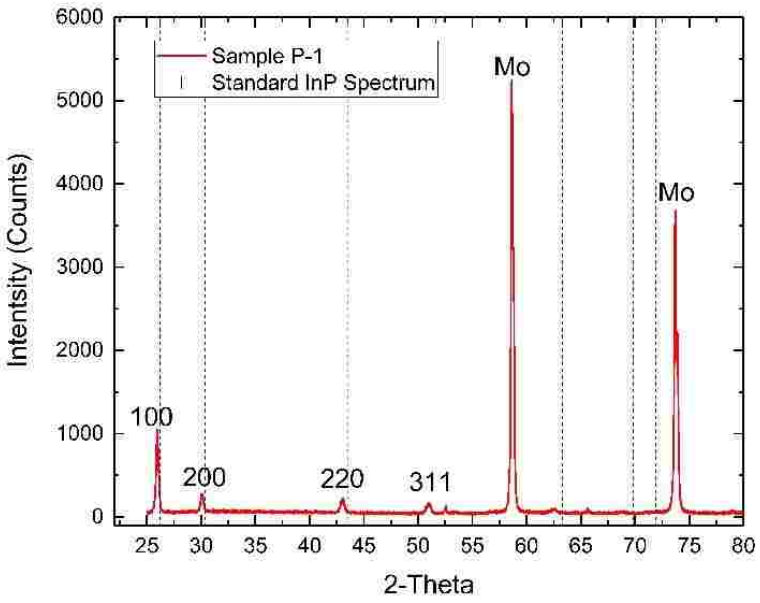

Fig. 3.1. XRD of Sample P-1 with labelled peaks for InP and Mo.

SEM was used to investigate surface details (discussed below) and with EDS capabilities determine the validity of the contamination hypothesis and identify the elemental makeup of the material. SEM was also used to show the surface structure and if a complete layer had formed. The SEM images are seen in Fig. 3.2 at magnifications of 170x (left) and 1,500x (right). The left

image shows that a complete layer was not obtained and that islanding is occurring. The islands appear to have a snowflake resemblance and are irregular in shape, but are similar in size. The islands appear spread out evenly throughout the sample with a rough island size of approximately 120µm, a more quantitative analysis is shown later with EDS. The right image in Fig. 3.2 shows the island features and appears to show polycrystalline features, such as grain boundaries and facets, which was expected.

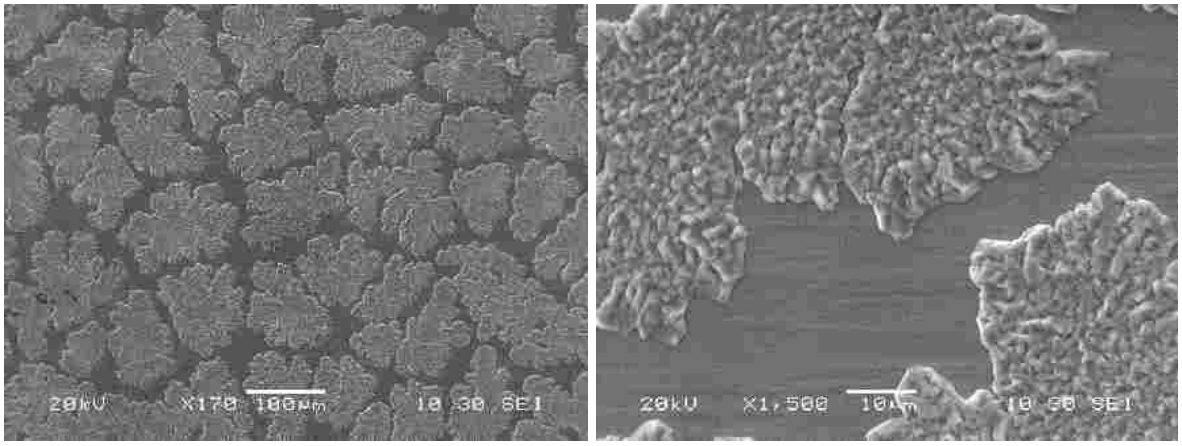

Fig. 3.2. SEM Images of Sample P-1 surface features and island structures.

EDS spectra was performed to confirm the presence of indium, phosphide, and if there was indeed arsenic contamination in Sample P-1. Fig. 3.3 shows the EDS Spectrum for Sample P-1 with labelled peak energies. The EDS results show the presences of indium, phosphorous, and molybdenum, which was expected, but also showed small levels of arsenic present in the sample. The EDS spectrum confirms the arsenic contamination. It appears that the Indium to Phosphorous ratio is not 1:1 based on height and width of the peaks. There appears to be more indium present than phosphorous, which means arsenic has potentially bonded with indium, taking the spot of some of the group V phosphorous atoms.

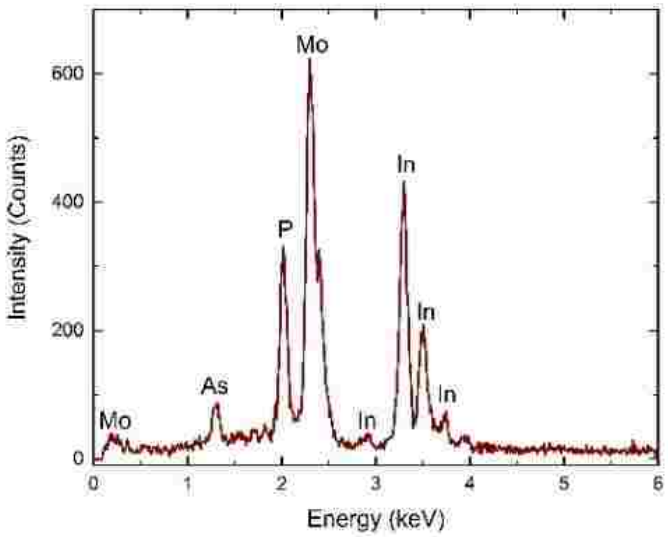

Fig. 3.3. EDS spectrum of sample P-1 with labelled elemental energies and intensities.

In addition to EDS Spectrum, EDS mapping was used to determine the location of the contamination present in the sample. Fig. 3.4 (a-e) shows EDS mapping for indium (a), arsenic (b), phosphorous (c), and molybdenum (d). Figure 2 (e) is the corresponding SEM image of Sample P-1. Based on further investigating the surface composition using EDS mapping, it was concluded that arsenic contamination is present, specifically where the crystal islands were formed, as seen in Fig. 3.4 (b). Indium, Fig. 3.4 (a) appears to be mainly present where the islands are located. Phosphorous seen in Fig. 3.4 (c) appears to be primarily located where the islands are, as and it should be noted that the excess phosphorous between the islands, is likely molybdenum due to the overlap in similar EDS peak intensities between Mo and P. The Mo map, Fig. 3.4 (d), shows Mo is located primarily where the islands are not covering. Based on the mapping of Sample P-1, the phosphorous intensity appears to be stronger on the islands as compared to arsenic. This verifies that phosphorous has a stronger presence and occupies more of the crystal structure than arsenic. This also verifies that there is arsenic contamination present, but based on intensity the phosphorous appears to make up a larger portion of the group V composition aspect.

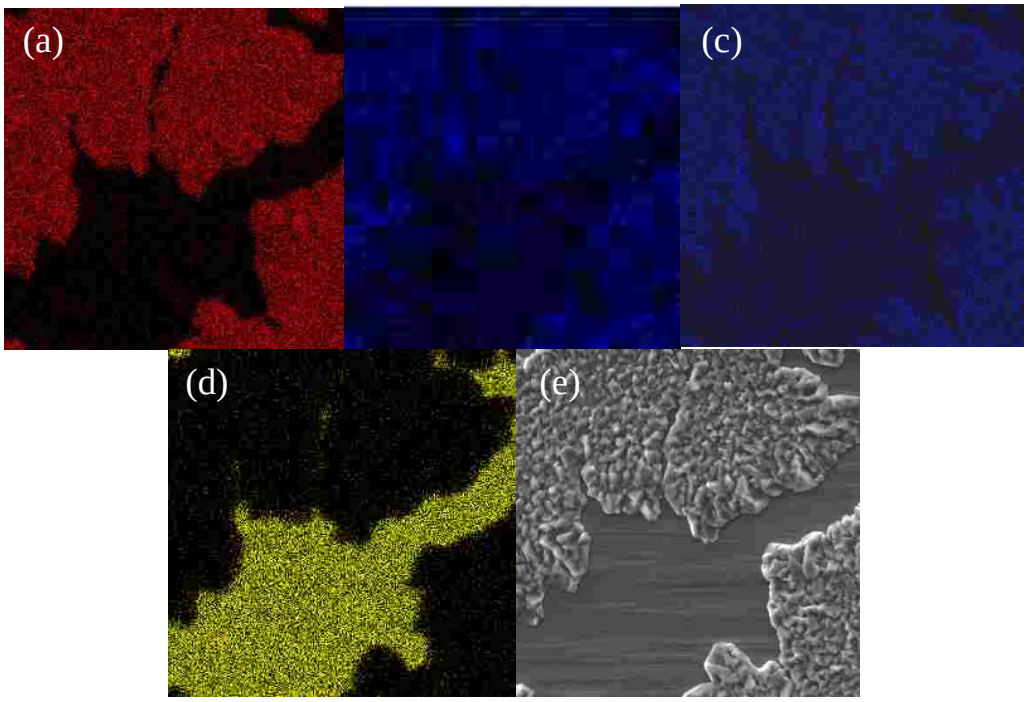

Fig. 3.4. EDS mapping of Sample P-1: (a) In, (b) As, (c) P, (d) Mo, (e) SEM Image.

To further investigate the ratio of phosphorous and arsenic to indium, the EDS spectrum quantitative results were analyzed. Table 3.2 shows the atom percentage of indium, phosphorous, and aresnic. The rest of the atom percentage is molybdenum. When comparing the group V ratio of phosphorous and arsenic, phosphorous makes up approximately 69.9% and arsenic makes up 30.1%. This is stlightly smaller than the ratio calculated based on lattice constant, but shows that phosphorous makes up a larger percentage of the group V component.

Table 3.2 Atom Percentage of Sample P-1

Element	Atom %	Group V Ratio %
Indium	33.91	-
Phosphorous	19.05	69.9
Arsenic	8.21	30.1

PL was conducted in order to determine the bandgap of Sample P-1 and compare with the known bandgap of InP. The known bandgap for InP is 1.34 eV, which corresponds to a

wavelength of 925 nm. Fig. 3.5 shows the PL results of Sample P-1, red curve, and for an uncontaminated InP Substrate, blue curve. As seen in Fig. 3.5, the wavelength for Sample P-1 is red-shifted. For Sample P-1, the PL measurement had a peak wavelength of 1116nm with a corresponding bandgap of 1.11eV. The decrease in bandgap agrees with the previous conclusions of contamination within the sample. Three PL measurements were taken at three different locations on the sample. Despite varying levels of intensities, uniformity was seen between all three points in terms of wavelengths, signifying that the sample had a consisted bandgap throughout. The lack of PL intensity of this sample could be due to the PL interaction volume.

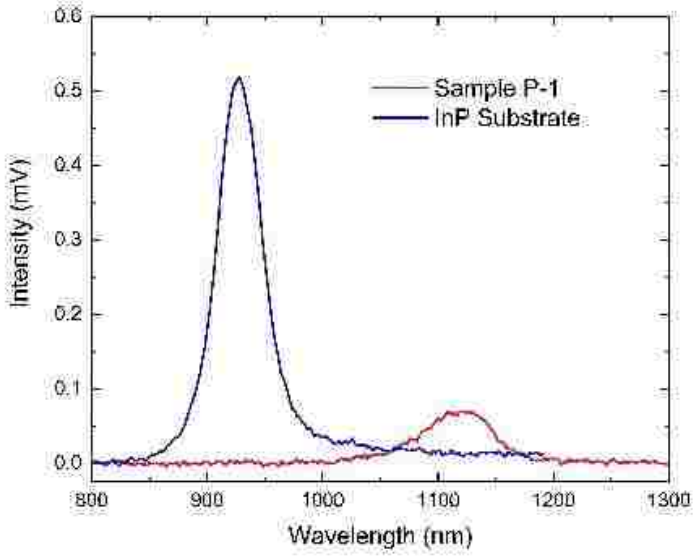

Fig. 3.5. PL results for Sample P-1 compared to InP substrate.

Sample P-1 showed that direct epitaxy of InP on Mo foil is possible at a temperature of 620° C. This sample did have arsenic contamination, which shows that a ternary is also possible on Mo foil. However, the SEM results showed that a uniform layer was not achieved and irregular shaped islands were present. The lattice constant was determined to be 5.94 A and the bandgap was 1.11eV, both representing contamination. EDS spectrum and mapping confirmed that arsenic contamination was present. The next sample was conducted with double the growth time to determine if this would increase surface coverage.

3.2 SAMPLE P-2 RESULTS AND DISCUSSION

Sample P-2 was the direct epitaxy growth of InP on Mo foil for two times the growth time of Sample P-1 with a total growth time of 98 minutes. The objective of this sample was to repeat the first sample growth to determine if increasing the growth time by double the amount would result in more surface coverage, as well as verifying if crystal structure was present and the alloy composition present. In addition to these objectives, the goal is to attempt a contamination free growth without arsenic. The InP Sample grown for 49 minutes in the previous study had an offset bandgap due to the arsenic contamination. Since the growth of Sample P-1, Arsenic had not been used and the reactor had since been coated with Phosphorus due to other growths utilizing phosphorous, preventing further significant contamination issues with samples P-2 and P-3.

XRD was completed to verify that Sample P-2 was InP. The XRD results are seen in Fig. 3.6. The blue vertical dash lines represents where the known InP peaks should be located [33]. Eighteen peaks were identified and labelled in Fig. 3.6, indicating the sample was polycrystalline. Three Mo peaks were identified and labelled in green. Using the XRD data and Vegard's law, the lattice constant for sample P-2 was determined to be 5.87 Å. The average lattice constant based on intensity was 5.85 Å. The lattice constants for this sample ranged from 5.84 to 5.87 Å. The lattice constant for Sample P-2 is extremely close to the known InP lattice constant of 5.86 Å. This shows the presence of InP and a lack of significant levels of contaminations. The increase in growth time from Sample P-1 to P-2 also lead to stronger peaks on the XRD plot, as well as more identified peaks, which was expected.

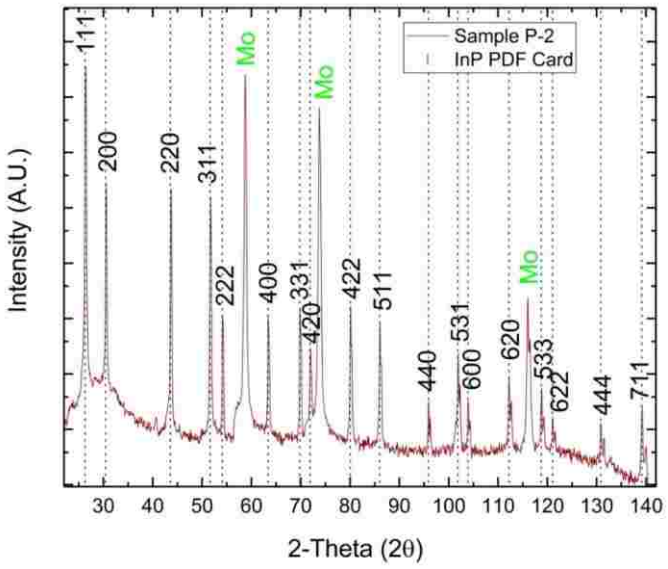

Fig. 3.6. XRD of Sample P-2 with labelled peaks for InP (18) and Mo (3).

The SEM was used to determine if islanding was still present with increase in growth time for Sample P-2. The SEM images are seen in Fig. 3.7. The left image shows the surface at a magnification of 330x and the right image shows a magnification of 1,500x. The left image appears to show an increase in surface coverage, but a complete layer has not formed. The right image shows that islanding was still present. The islands are much smaller in size about 6 micrometers in diameter, but more surface coverage appears to be present. The islands are very segregated, but are fairly similar in size throughout the sample. It also appears that polycrystalline features are present. The islands are different from the Sample P-1 islands. These are popcorn-like structures, whereas P-1 had snowflake-like structures, and appear to be coalescing.

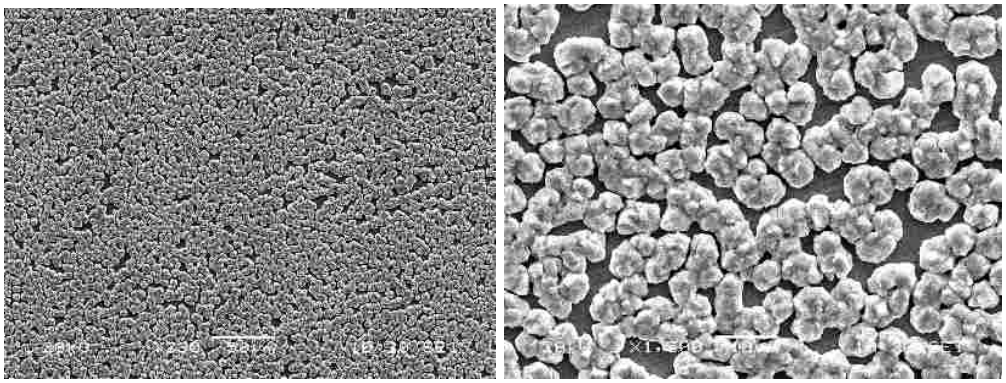

Fig. 3.7. SEM images of Sample P-2 surface features and coverage, left: magnification of 330x and right: magnification 1,500x.

EDS was used to determine the elemental composition of Sample P-2 and to verify the sample was contamination free. The EDS spectrum for Sample P-2 is seen in Fig. 3.8. The spectrum showed significant amounts of indium and phosphorus, which was expected. Also, molybdenum was detected in smaller amounts than sample P-1 probably due to the increase in surface coverage blocking the signal from reaching more of the substrate. Small traces of carbon were also detected and could be an artifact due to organic contamination from the EDS machine. The EDS detector has difficulties distinguishing between Mo and P energies, which is why the peak at approximately 2 keV is labelled P and Mo. Based on other tests, this peak is believed to be phosphorous. Additionally, there was no arsenic detected by the EDS machine, confirming the lack of contamination. The indium to phosphide ratio appears to be closer to 1:1 than in Sample P-1.

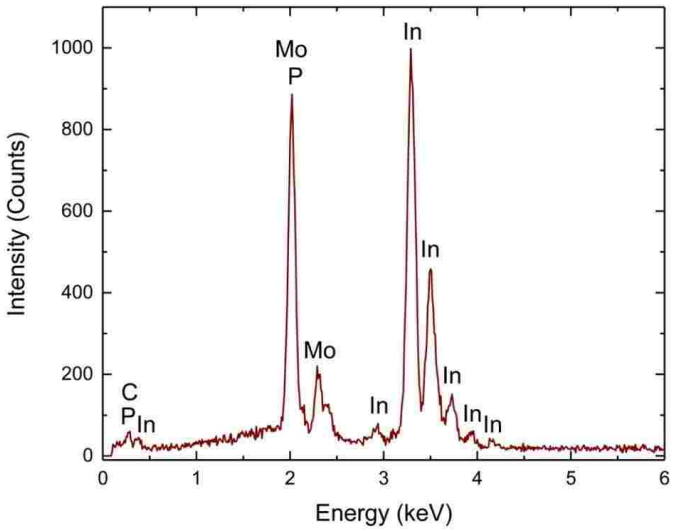

Fig. 3.8. EDS Spectrum of Sample P-2 with labelled energy peaks.

EDS Mapping was also conducted on Sample P-2 to determine the spatial orientation of the elements present in the sample. The results are seen in Fig. 3.9 (a-e), with EDS maps of Mo, C, In, P and corresponding SEM image. EDS mapping showed the islands consisted of mainly In and P, which was expected. Mo was detected around the islands. There was a mild spatial correlation of carbon incorporation with the islands, indicating a small presence of organic contamination and that the carbon could be replacing some of the indium and phosphorous atoms.

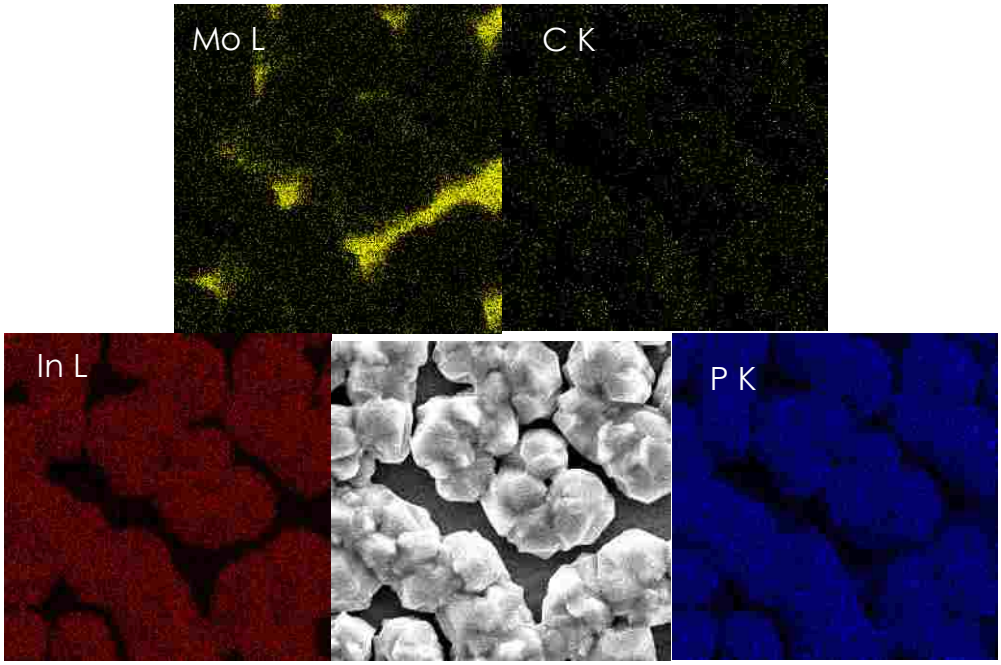

Fig. 3.9. EDS Mapping Results for Sample P-2.

EDS “point and shoot” function was used to gain more insight on specific elemental composition and to determine the ratio of the group V element to the group III element at specific x-y locations in the image. This method was conducted for three points, one on the Mo foil, point 1, and two on the islands, points 2 and 3. The location of these points are seen in Fig. 3.10. The atom percentage results are seen in Table 3.3. The remaining atom percentage is minimal amounts of organic contamination. Points 2 and 3 had very similar spectrums, both had more carbon detected than point 1. Points 2 and 3 also had larger amounts of P and In, with detection of Mo, due to the thickness of the islands preventing the EDS beam from reaching the substrate. For points 2 and 3, there was slightly more indium than phosphorous and just under a 1:1 ratio for In to P for these points on the islands, indicating polycrystalline results. This was closer than the ratio for In:P in sample P-1 due to the lack of contamination. Even though point 1 was taken on the substrate, there were still large amounts of P and In, which could either indicate a slight drift in the EDS detector beam or a potential small layer of InP growth.

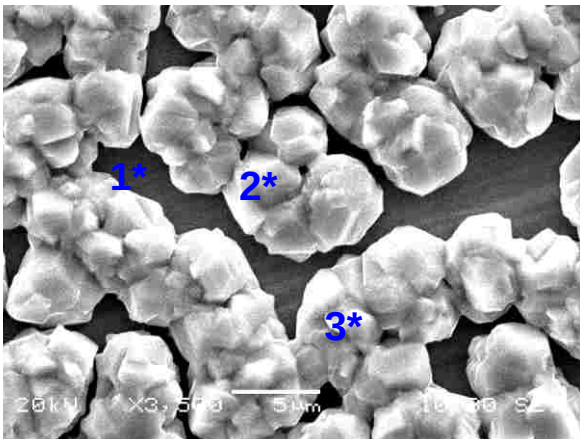

Fig. 3.10. EDS Point and Shoot for Sample P-2 with locations of the points taken for analysis.

Table 3.3: Atom Percentage of Specific Location Analysis for Sample P-2

Point #	C	In	P	In:P Ratio	Mo
1	-	32.65	24.88	-	42.47
2	34.75	33.54	30.64	1:0.91	-
3	35.13	33.05	29.82	1:0.90	-

Sample P-2 was grown for 98 minutes, which was two times the growth of Sample P-1. This sample contained no contamination, but still had islanding present. It appears that the increase in growth time also increased the surface coverage, which was expected. The islands on this sample were different from Sample P-1. This sample had rounder, popcorn like islands, whereas the first sample had more snowflake like structures. XRD results showed the similarities with the known InP peaks. The lattice constant and bandgap aligned closely with the known bandgap and lattice constant of InP. PL for samples P-2 and P-3 will be discussed in section 3.4 to show the slight differences between the two samples.

3.3 SAMPLE P-3 RESULTS AND DISCUSSION

Sample P-3 was the direct epitaxy growth of InP on Mo for 147 minutes, which was three times the growth time of Sample P-1. The purpose of the 3x growth time (147 minutes) was to determine if increasing the growth time further than Sample P-2 would increase surface coverage and if a complete layer would form. XRD was used to determine the lattice constant and if the

lattice planes match up with the known InP peaks. The XRD results are seen in Fig. 3.11, showing that 18 crystal planes were detected, confirming polycrystalline growth. These 18 peaks aligned closely with the known InP polycrystalline XRD peaks, represented by the blued vertical dash lines [33]. The strongest peaks included, 111, 200, 220, and 311. The average lattice constant for all peaks was 5.87 Å, which was very close to the known InP lattice constant of 5.86 Å. If taking into account intensity per lattice plane, the lattice constant was closer to 5.85 Å, which is slightly lower than the known InP lattice constant. However, there was not a significant amount of contamination detected by the EDS machine. Additionally, the XRD results for Sample P-3 were very similar to the results for Sample P-2.

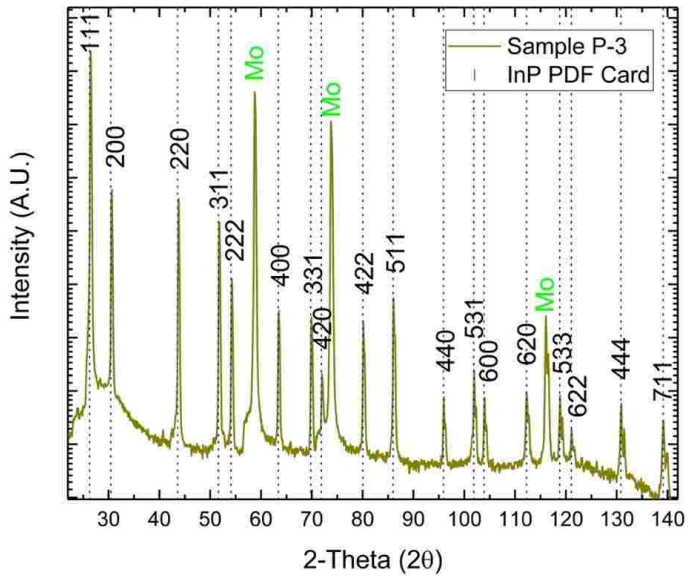

Fig. 3.11. XRD results for Sample P-3 with labelled peaks for InP and Mo.

SEM was used to investigate the surface and determine if islanding was still present with the increase in growth time. SEM images are seen in Fig. 3.12. The left image shows that islanding is still present. However, these islands are much larger in size compared to Sample P-2 and are round oval shapes. This sample appears to have more surface coverage than Sample P-1, but less than Sample P-2. Surface coverage analysis will be discussed later on in the next section in this chapter. The left image shows that the island size varied throughout the sample, anywhere from 50 micrometers to 100 micrometers. This image also shows the progress of the Volmer Weber with the increase in growth time as compared to Sample P-1 has led to increase in steps towards

merging of the islands. The middle image in Fig. 3.12 shows the polycrystalline features of Sample P-3. The right image depicts the increase in facet size near the edge of the islands as compared to the middle of the islands. The middle of these islands appears similar to the islands present in Sample P-1.

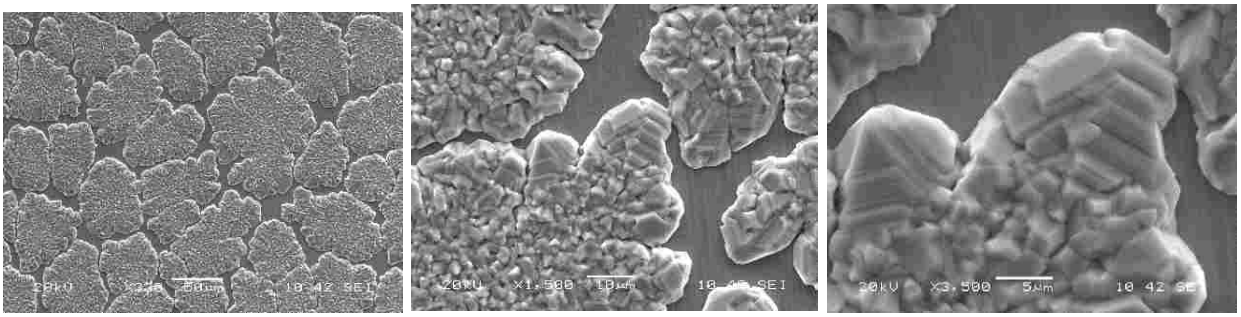

Fig. 3.12. SEM Images of Sample P-3.

EDS Spectrum was conducted to confirm that indium phosphide was present, while checking for potential contamination. EDS Spectrum results are seen in Fig. 3.13 showing strong P and In peaks, which was expected. The Mo peak is lower than Sample P-1 due to the thickness of the layer and less of the substrate being detected. As previous stated the peak labelled Mo and P at approximately the 2 keV spot is believed to be phosphorous. Additionally, some organic contamination in the form of carbon was detected. There also appears to be slightly more indium present than phosphorous, based on peak height and width.

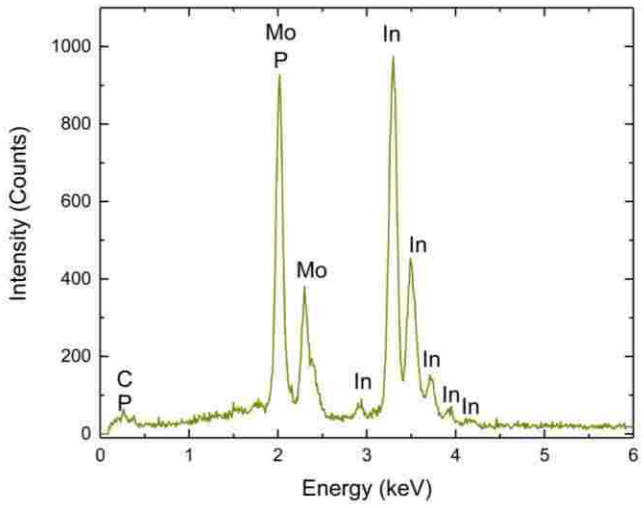

Fig. 3.13 EDS Spectrum of Sample P-3 with labelled energy peaks.

EDS mapping was also used to analyze Sample P-3 to gain insight on elemental location and the results are seen in Fig. 3.14 with the corresponding SEM image. EDS mapping showed In and P where the islands were located and Mo on the substrate. Some phosphorous was detected in the on the substrate, this is likely due to the detector having difficulties distinguishing between P and Mo peaks. EDS Mapping confirmed the presence of InP crystal growth.

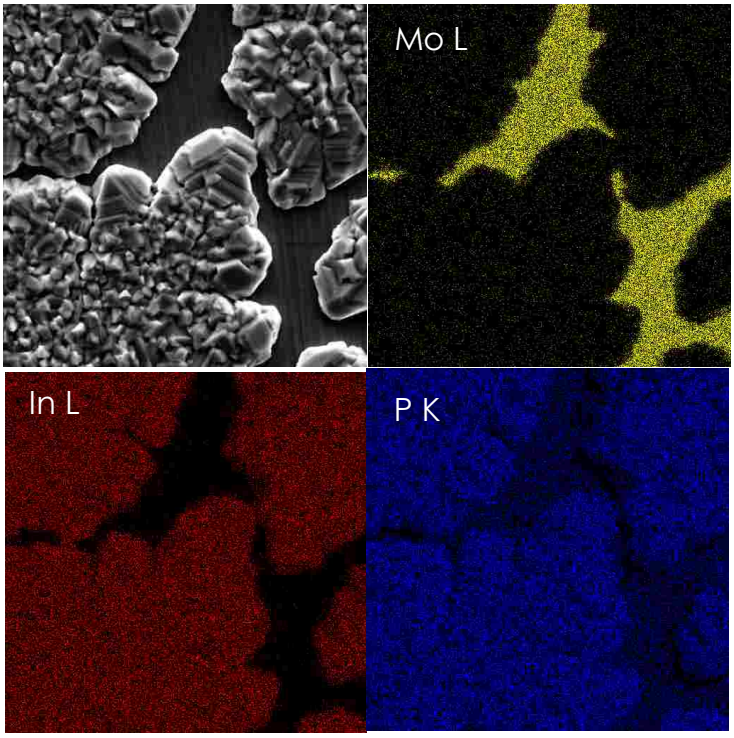

Fig. 3.14. EDS Mapping of Sample P-3.

The EDS "Point and Shoot" function was also used here to determine the ratio of In to P and obtain a more specific elemental composition analysis on the islands. There were four points taken using this method, one on the Mo foil, point 4, two on the edges of the island, point 1 and 2, and one on the middle of the island, point 3. Fig. 3.15 shows the locations of the points on the sample. Points 1,2, and 3 have very similar spectrum results. However, point 2 have slightly higher P and intensity. Point 4 had a strong Mo intensity, which was expected. Table 3.4 has the atomic percentage for each point taken. For the ratio In:P, In had a larger percentage compared to phosphorous. Point 2 had the closest ratio to 1:1. The indium percentage was consisted with each

point taken on the island. Whereas, the phosphorous varied slightly. Overall, there was more indium than phosphorus present, which was consistent with EDS spectrum results. Also, the carbon atom percentage did make up a large portion of the percentage, which could be a resulting artifact from the EDS machine.

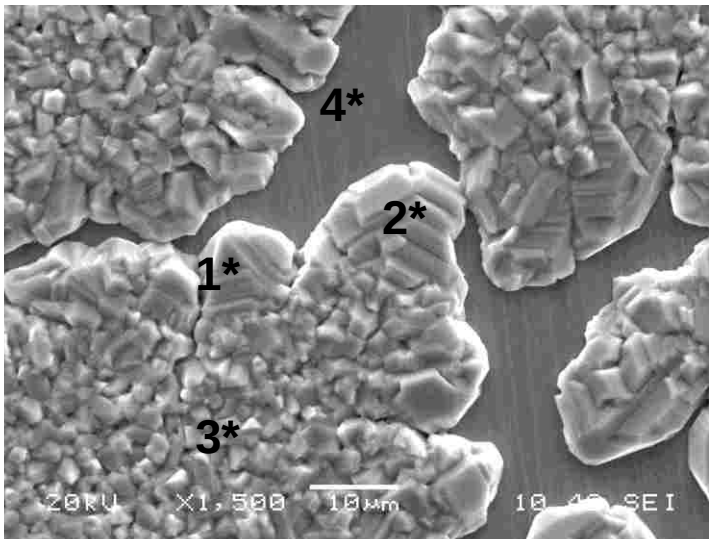

Fig. 3.15. EDS Point and Shoot locations for Sample P-3.

Table: 3.4 Atom Percentage of Specific Location Analysis of Sample P-3

Point #	C	In	P	In:P Ratio	Mo
1	27.96	38.31	33.74	1:0.88	-
2	24.66	38.94	36.40	1:0.93	-
3	27.38	38.68	33.94	1:0.88	-
4	-	-	7.99	-	92.01

Sample P-3 was grown for three times the growth time of Sample P-1, but still had islanding present. This sample did not contain any arsenic contamination. The islands were similar in shape to Sample P-1, but covered more area. XRD results showed that 18 peaks were present, along with polycrystalline structure. The lattice constant and bandgap aligned closely with the known values for InP.

3.4 GROWTH TIME COMPARISON FOR SAMPLES P-1, P-2 AND P-3

The main purpose of this section was to determine how the growth time affected the direct growth of InP on Mo foil, more specially, determine if there is a correlation between growth time and surface coverage and the effect on XRD and PL peaks and intensities, PL. Fig. 3.16 shows the XRD comparison for samples P-2 and P-3. Each sample had 18 peaks that aligned with the known InP planes, indicated by the vertical blue dash line. The green dash line is the Mo peaks, which included three identified Mo peaks. Sample P-1 was not included due to the offset peaks from the arsenic contamination. Samples P-2 and P-3 had very similar XRD plots, with the strongest peaks being 111, 200, 220, and 311 for both samples. In addition, they also had more noticeable peaks than Sample P-1.

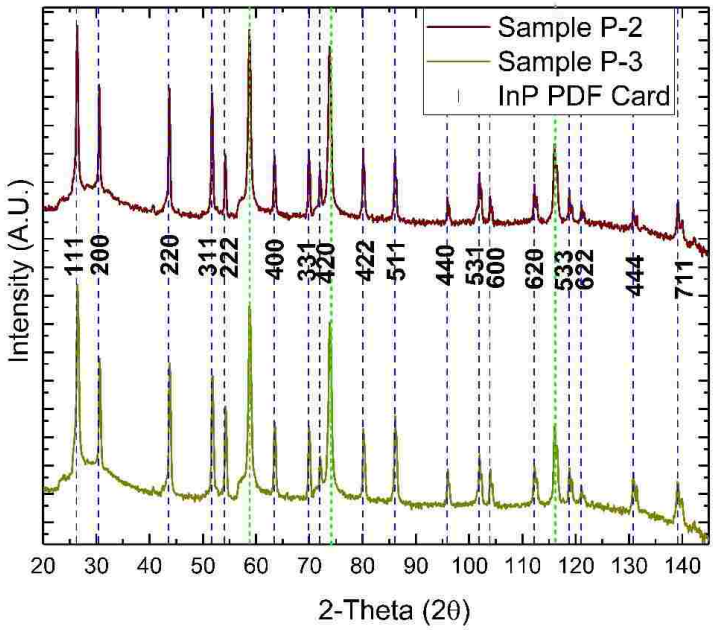

Fig. 3.16. XRD results comparison for Sample P-2 and P-3 with labelled crystal planes.

PL comparison results for P-2 and P-3 are seen in Fig. 3.17. Sample P-1 was not included because of the offset in wavelength due to the arsenic contamination. Both P-2 and P-3 had similar bandgaps to the known InP bandgap. However, the full-width half-maximum (FWHM) and intensity of Sample P-2 (25nm) aligned closer with the single crystalline InP wafer, which had a FWHM of 24nm, than Sample P-3, which had a FWHM value of 26nm. The PL results for

these samples show that high quality polycrystalline features are possible with the direct growth of InP on Mo foils.

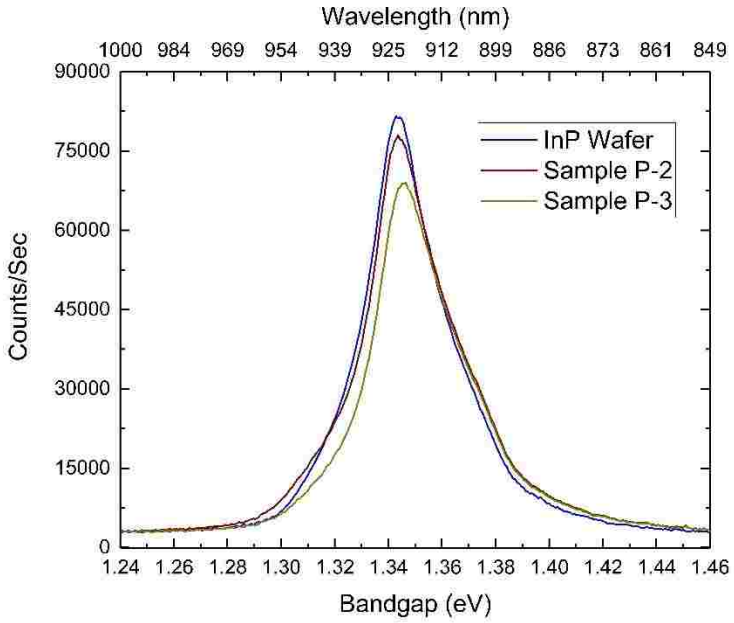

Fig. 3.17. PL results comparison for Samples P-2 and P-3.

SEM comparison of all three samples was conducted and the results are seen in Fig. 3.20 for two magnifications of 330x and 1,500x. At a magnification of 330x, islanding was present for all three samples. Sample P-1 appeared to have the smallest surface coverage. Sample P-2 appeared to have slightly larger surface coverage than Sample P-3. The SEM images at a magnification of 1,500x shows that polycrystalline features are present in each of the three samples. Sample P-1 had the largest islands with a dendritic shape. Sample P-2 had islands that were balled up and were the smallest in size as compared to the other two samples, which could indicate a potential surface issue. However, this islands were all similar sizes. Sample P-3 had larger islands than Sample P-2, but the islands were not all the same size. At a magnification of 1,500x comparisons, Sample P-1 and P-3 have similar crystal structure, except Sample P-3 had longer features near the edges. It appears that the increase in growth time did lead to more surface coverage.

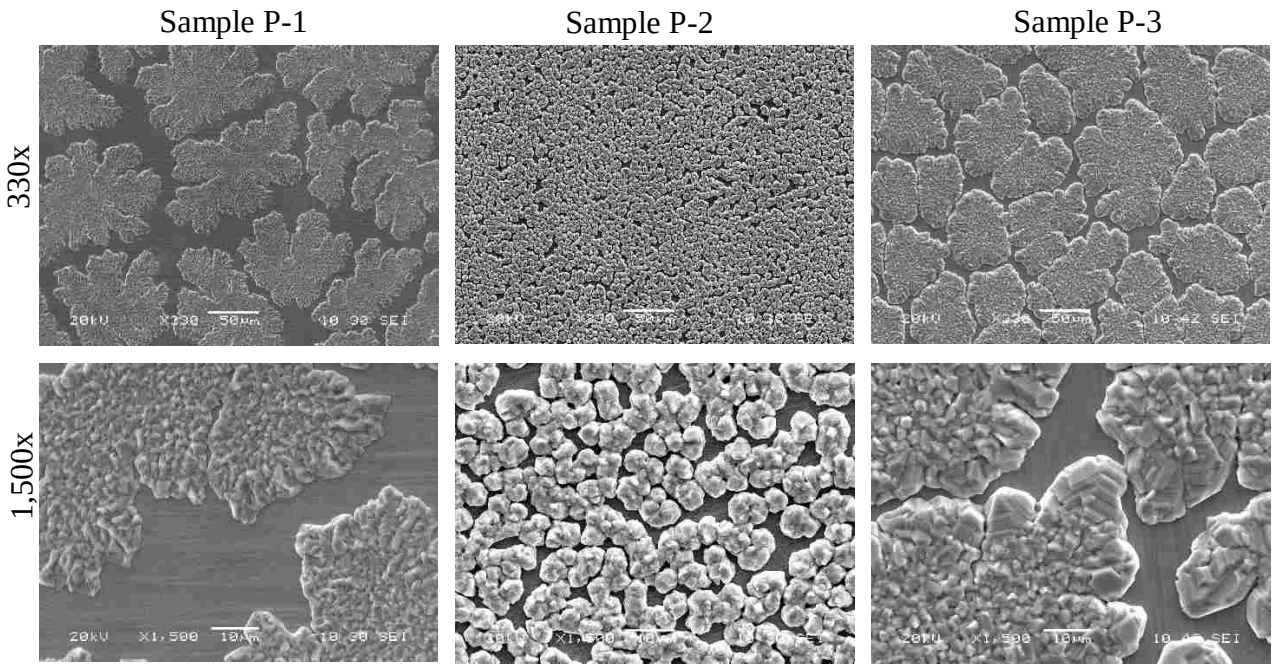

Fig. 3.18. SEM Comparison for Samples P-1, P-2, and P-3 for magnifications of 330x and 1,500x.

There was not a significant difference between Sample P-2 and P-3, but there was a large difference between P-1 and P-2. ImageJ was used to determine the surface coverage percentage for each sample. The results for surface coverage are seen in table 3.5. Sample P-1 had a surface coverage of approximately 68%, Sample P-2 had 78%, and Sample P-3 had 76%. This confirms that P-2 and P-3 Samples had similar surface coverage percentage and were both larger than the surface coverage of Sample P-1, but Sample P-2 had slightly larger coverage than P-3.

The increase in growth time also lead to stronger peaks on the XRD and more identified peaks, which was expected, as well as better alignment with the PL curve. Sample P-1 did have arsenic contamination, whereas the other two samples, P-2 and P-3, did not have contamination present. The results for lattice constant and bandgap for the three samples are seen in Table 3.5, along with growth time, In:P ratio and island size.

Table 3.5 Comparison of Sample P-1, P-2, and P-3

	Sample P-1	Sample P-2	Sample P-3
Growth Time (min)	49	98	17
Lattice Constant (Å)	5.94	5.85	5.85
Bandgap (eV)	1.11	1.34	1.35
Surface Coverage	~68%	~78%	~76%
In:P Ratio	1:0.57	1: 0.90- 0.91	1: 0.88-0.93
Island Size (µm)	~120	~6	~100

The lattice constant for Sample P-2 and P-3 was the same, but due to the contamination, Sample P-1 had a larger lattice constant of 5.94 Å. The PL results were similar for Sample P-2 and P-3. Sample P-2's bandgap aligned with the accepted bandgap and P-3's bandgap was slightly larger by 0.01 eV, whereas Sample P-1 had a bandgap of 1.11 eV. Surface coverage did increase with growth time between Sample P-1 and P-2 by approximately 10%. There was only a slight difference in surface coverage between Sample P-2 and P-3 of approximately 2%, despite an increase in growth time from 98 minutes to 147 minutes. The In:P ratio was 1 to 0.57 for Sample P-1, but closer to 1 to 1 for Samples P-2 and P-3. With Sample P-2, the range for P was more consistent, whereas for Sample P-3's, the P portion ranged from 0.88 to 0.93. The average island size for Sample P-1 was the largest with an average of 120µm. Sample P-3 was close with an average island size of 100µm, whereas Sample P-2 had the smallest island sizes, which were 20 times smaller than islands of Sample P-1. The difference in island size can be seen in Fig. 3.18. Despite the increase in growth time by three times the first growth, a uniform layer was still not achieved. Based on this outcome, other parameters will be investigated, such as the temperature or altering the surface energy, which could be affecting the surface coverage and therefore will be the next variables investigated. Due to the similarities between Sample P-2 PL results and the InP substrate, a growth time of 98 minutes is preferred over the 147 minutes.

CHAPTER 4

DIRECT EPITAXIAL GROWTH OF INDIUM ARESNIDE ON MOLYBDENUM FOIL

The compound, InAs, is extremely important in applications involving optoelectronic devices that require long-wavelength detection capabilities [12]. Applications of low bandgaps and mid-infrared capabilities, besides solar cells, include highly sensitive detectors used for picking up small traces of toxic gases and pollution or for monitoring chemical and industrial processes, and lasers used for military communications or biomedical purposes [34] [35]. Mid-infrared lasers are also useful for remote sensing and molecular spectroscopy [35]. Other optoelectronic devices that could benefit from the use of low bandgap materials are infrared photodetectors and modern optical telecommunication [13, 29]. The mid-infrared (MIR) is included in the long-wavelength infrared spectrum and includes the region of 2μm-20μm [34, 35]. The MIR region has an increased absorption strength compared to near-infrared that creates more sensitivity when detecting trace amounts of atoms [34]. InAs has a low bandgap of 0.36 eV at room temperature, and this relatively low bandgap makes InAs very suitable for applications involving aforementioned photodetectors with wavelengths in the range of 1μm to 3μm [8].

Typically for long-wavelength devices, GaAs and InP are used as substrates. InP is useful for optical fibers because the lattice-matched bandgaps provide for alloys with low dispersion [36]. GaAs is preferred for devices that require higher efficiencies. GaAs and InP substrates used for mid-IR lasers typically have lower cost and more developed fabrication processes associated with them, as compared to InAs. However, InAs is more suitable for reaching long wavelengths past the 2μm mark [35]. Originally, these mid-infrared devices had poor performance in terms of quantum efficiency and operating temperature, but with improvements made in the epitaxy growth processes, such as with MOCVD and MBE, InAs material quality has improved [35]. InAs is more expensive than both InP and GaAs, and rarer due to its lack of availability. Despite these disadvantages, InAs has useful characteristics such as a high electron mobility, narrow bandgap, and electro-optical properties [37]. If the costs associated with InAs materials could be lowered, the use of this low bandgap material could be exploited and expanded further. In this

chapter, the direct growth of InAs on Mo is explored in an effort to decrease the costs associated with InAs substrates. An additional sample was growth under the same conditions as InP in terms of temperature, precursors, and pressure for Indium Arsenide.

4.1 SAMPLE A-1 RESULTS AND DISCUSSION

Similar to the InP study in Chapter 3, an investigation of mechanical properties took place using material characterization for InAs. Sample A-1 was also grown using the same direct growth method as the previous InP samples. The temperature and pressure settings used for the InP samples were used for this sample. This sample also had a growth time of 49 minutes, but involved the direct MOCVD growth of a different binary, Indium Arsenide, on Mo foil. The purpose of this sample was to investigate the feasibility of also growing additional binaries, such as InAs, in a two-dimensional architecture. Sample A-1 was grown after the reactor chamber was cleaned to minimize phosphorous contamination. The cleaning process included replacing the InP substrate with a clean one and flowing InAs without a sample loaded in order to coat the other surfaces with InAs thus suppressing the desorption of any phosphorous that could have remained from previous growths. The goal of sample A-1 was to grow only InAs, removing the potential of phosphorous contamination and to determine how effective this growth process would be for InAs.

XRD was conducted on sample A-1 for lattice constant determination. Fig. 4.1 shows the XRD plot from Sample A-1. The peaks labelled are compared to the InAs PDF card and line up with known peak of InAs, while the remaining peaks are consistent with the known Molybdenum peaks and are labelled in green [38]. A significant number of the accepted InAs x-ray peaks line up with the XRD data obtained from Sample A-1. There were 12 InAs identified peaks for this sample and 2 Mo peaks. The lattice constant calculated based on the lattice planes was determined to be 6.04 Å, which is very similar to the known InAs lattice constant of 6.05Å [12]. The XRD data for Sample A-1 confirms the presence of InAs, and a particular lack of any contaminants. The strongest peaks indicated diffraction from the 100, 220, 311 and 622 planes. These results also show that Sample A-1 is polycrystalline material because of the different crystal planes that were identified.

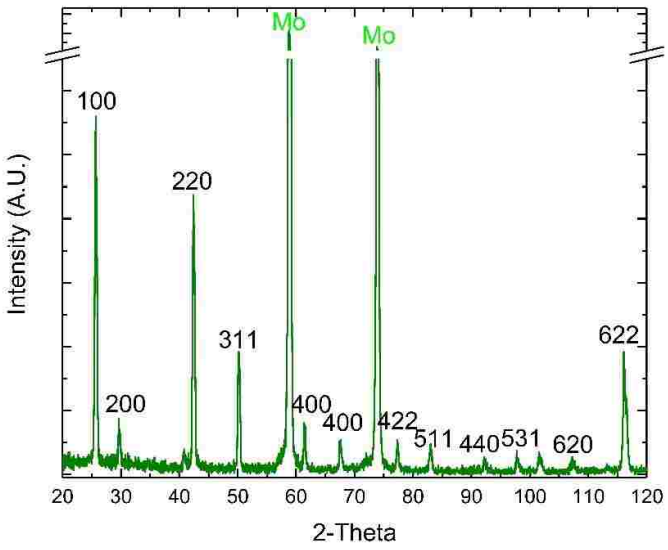

Fig. 4.1. XRD Results of Sample A-1 with labelled peaks.

SEM was conducted to investigate the surface to better understand the growth morphology in terms of islands versus 2D layer growth. The results are seen in Fig. 4.2. The image shows islanding of crystals, which ranged in diameter from 7.9μm to 22.2μm, as determined by Origin analysis. The left image in Fig. 4.2 shows the islands cover the majority of the molybdenum foil fairly uniformly. The crystal size for Sample A-1 was approximately five times smaller than that of Sample P-1. The average distance between particles for Sample A-1 was determined to be 7.06μm and consisted of similar oblong semi- hemispherical shapes. Whereas, Sample P-1 had more irregular snowflake-like shapes. These crystals were similar in size throughout the surface and uniformly distributed. The 330x image (left) shows that the spatial similarities between the islands and 1,500x (right) shows the polycrystalline features of the sample.

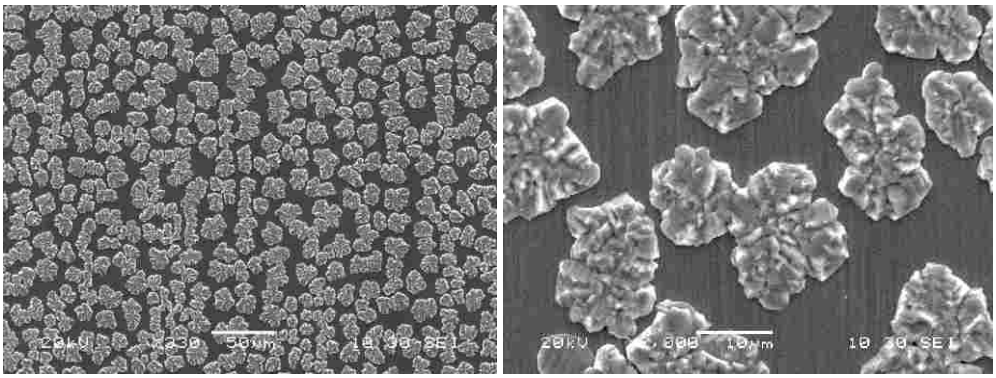

Fig. 4.2 SEM images of Sample A-1

When reviewing the EDS spectrum of Sample A-1, Fig. 4.3, phosphorous was not detected, because this measurement technique is sensitive to elemental composition, it is noted that there is no significant phosphorous contamination or any other contamination present in this sample. The EDS spectrum, however, confirm the presence of arsenic, indium, and molybdenum. The spectrum also shows the relative similarity in intensities of arsenic to indium. Based on peak height and width of In and As peaks in the EDS full spectrum, it was qualitatively determined the ratio of indium to arsenic is fairly close to a 1:1 ratio, showing promising results for InAs purity and direct In-As bonding. The Mo peak had the largest intensity, which indicates that a large portion of the surface is not covered and the InAs layer is not particularly thick.

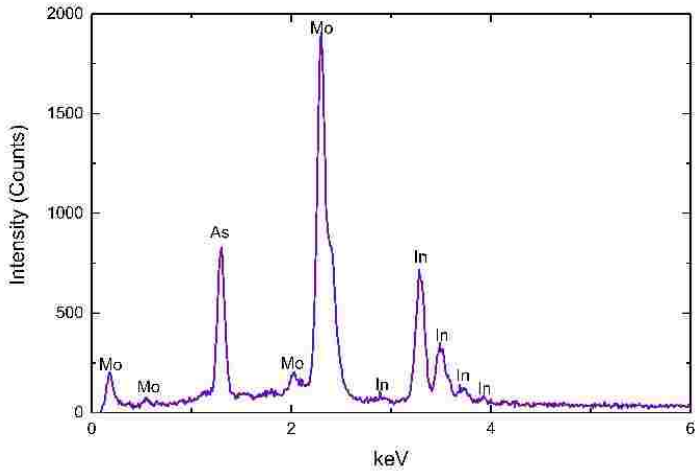

Fig. 4.3. EDS Spectrum for Sample A-1 with labelled peak intensities.

EDS Mapping was used to determine the spatial distribution of elemental composition and if contamination was present elsewhere on the sample. The results are seen in Fig. 4.4 (a-d). The presence of phosphorous was also checked with EDS to ensure that the material was binary InAs and not a ternary. The In EDS map, Fig. 4.4 (a), shows a strong indium signal where the islands are located. Arsenic is also detected on the islands, as shown in Fig. 4.4 (b). Due to the proximity of the molybdenum peak to the phosphorous peak it is difficult to distinguish between the two. However, based on the EDS mapping and the spatial similarities to the Mo EDS map, Fig. 4.4 (c), it is assumed that the phosphorous detected around the islands is in fact Mo, but there are a few phosphorus points detected on the islands that do not appear on the Mo map. This indicates a possible very slight contamination of phosphorous. Using Vegard's Law to determine the level

of contamination, the resulting composition is found to be $InAs_{0.95}P_{0.05}$. Therefore, based on EDS mapping and spectra, it is believed that the islands are composed of mainly InAs with a slight P contamination.

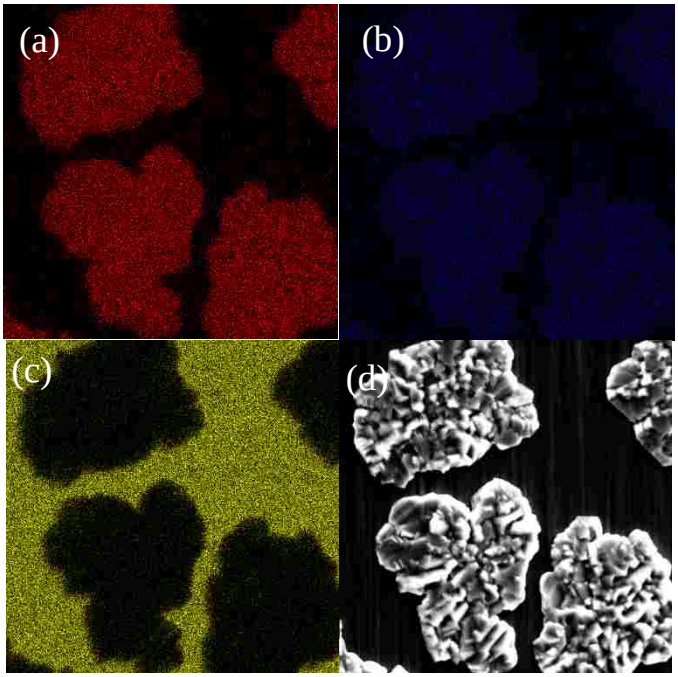

Fig. 4.4. EDS mapping of sample A-1: (a) In (b) As (c) Mo (d) SEM.

However, when isolating the location of the measurements taken by utilizing the "Point and Shoot" function of the EDS tool for four EDS point measurements, as seen in Fig. 4.5, the ratio of indium to arsenic is closer to 1:1 for the points taken on the islands (points 2-4) This is based on the atomic percentages represented in table 4.1. Sample A-1 had the closet 1:1 ratio for group V to group III with a 1: 0.99 ratio, as compared to the InP samples, which had slightly more indium present than phosphorous. Point 1 was taken on the substrate, which confirmed it was molybdenum. The other three points, located on one of the crystals at varying locations, included only a small percentage of Mo and did not pick up any traces of phosphorous. Therefore, if there was a small portion of phosphorous present, it was not large enough to impact the sample elemental analysis. Point 2 had a slightly higher amount of molybdenum percentage, which could be due to the lower height at the location of this point as it appears on the SEM image.

However, the EDS point measurements on the crystal showed the presence of a large amount of organic contamination in the form of carbon, which makes up the remaining portion of the atomic percentage data seen in Table I below. This could be an artifact from the SEM imaging tool due to the higher magnification or could be attributed to the increase likelihood of carbon impurity since the growth temperature was above 600° C, as this has been shown in literature [8].

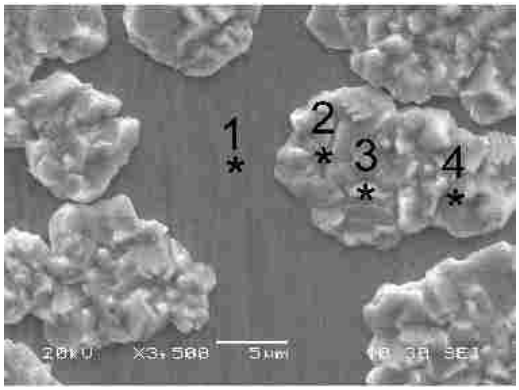

Fig. 4.5. Corresponding SEM Image for EDS P&S of Sample A-1 showing the location of the points used for further elemental analysis.

Table 4.1 Atomic Percentages for Specific Point Measurement of Sample A-1

Point #	Indium	Arsenic	In:As Ratio	Molybdenum	Carbon
1	0	0	-	100	0
2	30.95	30.53	1:0.98	6.43	32.09
3	32.24	32.56	0.99:1	1.80	33.23
4	38.72	36.89	1:0.95	2.51	21.88

Lastly, AFM using the non-contact tapping mode was performed on Sample A-1 to investigate the surface roughness, seen in Fig. 4.6. The surface was found to be extremely rough having a roughness mean square (RMS) value of 707.46 nm, in comparison to epi-ready surfaces. In one study, a 100nm thick buffer layer of InAs was grown using MBE on an InAs

substrate and AFM was used to determine the RMS value, which ranged between 0.6 nm to 4.1 nm for the different samples [39]. The Volmer-Weber growth present with this InAs sample associated with the lattice mismatch to the substrate could have led to the extreme surface roughness, since this growth results in 3D islands [32]. To limit the surface roughness, growth time could be increased to improve surface coverage, in addition to decreasing the growth temperature because with MOCVD, lowering the growth temperature improves surface coverage values, but lowers crystalline quality [16]. Adding a lattice buffer could help reduce the strain between the Mo foil and the InAs layer [29].

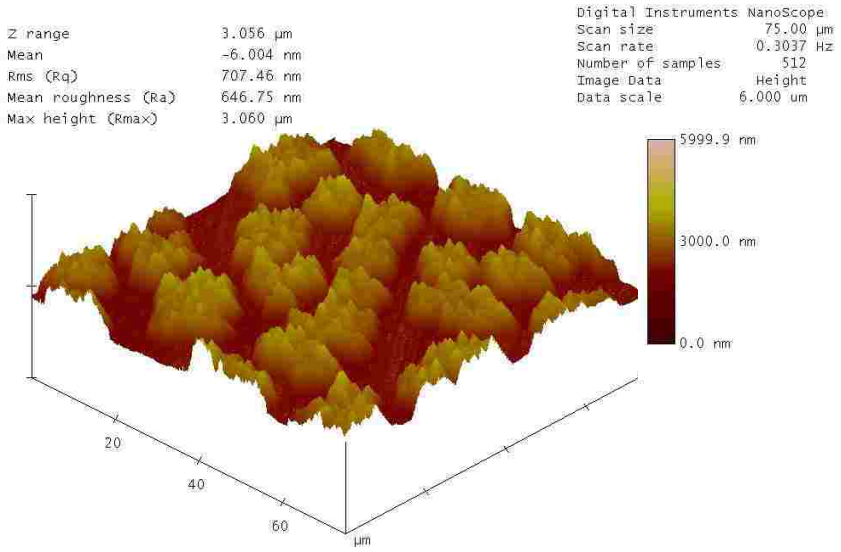

Fig. 4.6. AFM results for Sample A-1 showing 3-d surface roughness with quantitative results.

To determine the surface percent coverage as in Chapter 3, ImageJ was used for Sample A-1. The results are seen in Fig. 4.7. The left image is the corresponding SEM image used for this analysis. The right image shows the results of using the "Analyze Particles" function in conjunction with the outline tool, which can identity and locate the number of islands. The percentage of area coverage for Sample A-1 was 55.3% with 46 islands identified in the region used for analysis. This surface coverage percentage was approximately 13% lower than the percentage for the InP Sample, P-1, which had a percentage of 68%. It is expected that an increase in growth time would increase surface coverage, based on the results from the InP sample set growth time study.

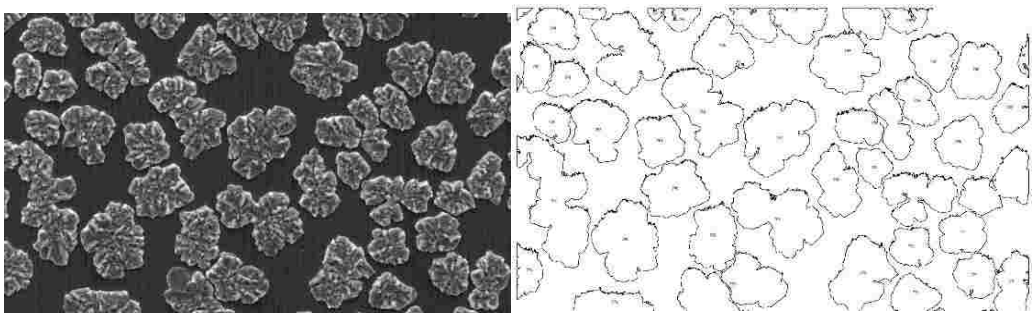

Fig. 4.7. Left image: SEM, Right Image: Island density and surface coverage of Sample A-1.

Even though islanding was present, the close 1:1 ratio shows that there is arsenic bound to indium and it is possible to directly grow, not only polycrystalline InP on molybdenum foil, but polycrystalline InAs as well. This sample had the closet 1:1 ratio for group III to V as compared to the InP samples. The lattice constant for the InAs sample was fairly close to the known InAs lattice constant, which was also observed with the InP samples. PL was not used on this sample because of the limitations of the detector not being able to reach the low bandgap. Surface coverage was lower for Sample A-1 as compared to Sample P-1, which had the same growth time of 49 minutes. However, sample A-1 had more identified and stronger peaks for XRD. InAs can be used for a solar cell device and is extremely useful for infrared devices that need a lower bandgap.

CHAPTER 5

CHARACTERIZATION STUDY OF ALUMINUM-INDUCED CRYSTALLIZATION OF GERMANIUM

Germanium is often used as the substrate in multijunction III-V solar cells to achieve high efficiencies above 40%. However, the cost associated with Ge substrates is still relatively high. Silicon substrates are considerably cheaper, but silicon has a low absorption coefficient and is limited in terms of being lattice matched to other semiconductor materials. Ge on the other hand has a lattice constant similar to GaAs and a low bandgap, which makes Ge well suited for a III-V bottom junction [4]. Substrates are typically the most expensive part of III-V solar cells [5]. Polycrystalline techniques of germanium are used to decrease the costs associated with a monocrystalline substrate. One particular technique of interest is the aluminum-induced crystallization (AIC) of germanium because of the lower stress and larger grain sizes associated with this process [14]. The AIC of Ge technique is investigated in this chapter in terms of characterizing the results from changing the ramp rate and set point temperatures.

Five samples were fabricated with the aluminum-induced crystallization process. All samples had a 2in wafer with 500nm of SiO_2 deposited on it, in addition to 50nm of aluminum, which is a typical aluminum thickness of AIC process, deposited on the SiO_2. Ramp rates were 1 °C/s and 0.1 °C/s, and set point temperatures were 480° C and 500° C. A lower ramp rate was chosen in order to decrease stress on the sample during layer transfer. These temperatures were chosen in order to promote crystalline growth. Germanium layer deposited on the Al layer varied between 200nm, 400nm, and 600nm. A thicker layer of germanium is preferred and increasing the germanium thickness gives insight into how this affects stress on the sample. The sample structure with corresponding layer thicknesses is seen in Fig. 5.1. This chapter discusses the characterization of these five samples to gain insight on the surface features and spatial elemental composition associated with the varying ramp rates and set point temperatures. The aluminum layer has not been etched off of these samples.

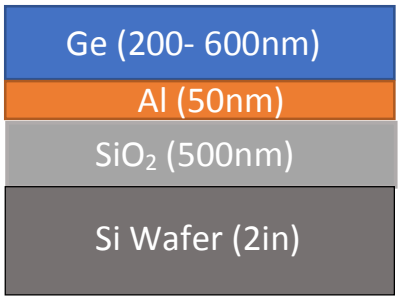

Fig. 5.1 Sample structure of aluminum-induced crystallization of germanium on silicon wafer with corresponding layer thicknesses.

The sample list is seen in Table 5.1. Two samples Al-1 and Al-2 had a set point temperature of 480° C and a ramp rate of 1°C/s, but different germanium thicknesses of 200nm and 600nm, respectively. A third sample, Al-3, had a set point of 500° C and a ramp rate of 1°C/s with a germanium layer thickness of 400nm. Both samples Al-4 and Al-5 had set point temperatures of 500° C and a ramp rate of 0.1 °C/s, but with germanium thicknesses of 200nm and 600 nm respectively.

Table 5.1 AIC-Ge Sample List and Parameters

Sample	Al	Ge	Set Point	Ramp Rate
Al-1	50 nm	200 nm	480° C	1 °C/s
Al-2	50 nm	600 nm	480° C	1 °C/s
Al-3	50 nm	400 nm	500° C	1 °C/s
Al-4	50 nm	200 nm	500° C	0.1 °C/s
Al-5	50 nm	600 nm	500° C	0.1 °C/s

5.1 SAMPLE A1-1 RESULTS AND DISCUSSION

Sample Al-1 had a 50nm aluminum thickness, 200nm germanium thickness, 480° C set point temperature, and a ramp rate of 1°/sec. SEM and EDS characterization techniques were conducted on this sample. SEM results are seen in Fig. 5.2 with magnifications of 1,600x and 23,000x. The left image shows the surface is covered in small spherical light spots, known as

hillocks, and irregular shaped dark spots. The right image in Fig. 5.2 shows a zoomed in image of the left image showing a side by side light spot and dark spot. The light spherical shape appears to be raised above the surface and the dark spot appears to be a valley feature.

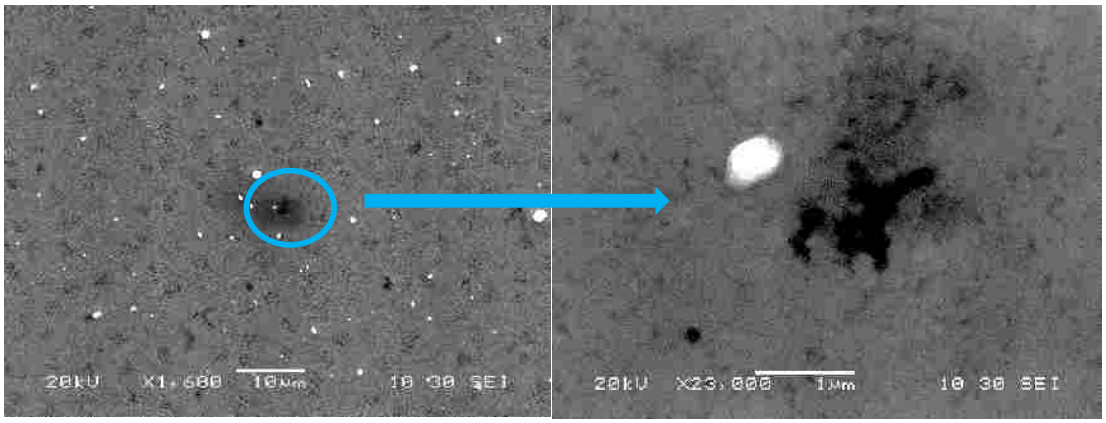

Fig. 5.2. SEM results left image: 1,600x and right image: 23,000x zoomed in on light and dark feature.

Additional SEM images are seen in Fig. 5.3. The left image shows the significant surface coverage of dark spots on the sample surface in addition to scattered round white spots, which appear distributed irregularly on the surface. The right image in Fig. 5.3 is a zoomed in version at a magnification of 7,500x showing additional dark spots, which appear to take a mesh-like shape, and a few light spots which are circular and oval in shape and appear to be clustered together throughout the sample. These images also show that the dark spots appear to be lower than the rest of the sample and the light spots are raised. Hillocks were also seen in another study of AIC of Ge [18].

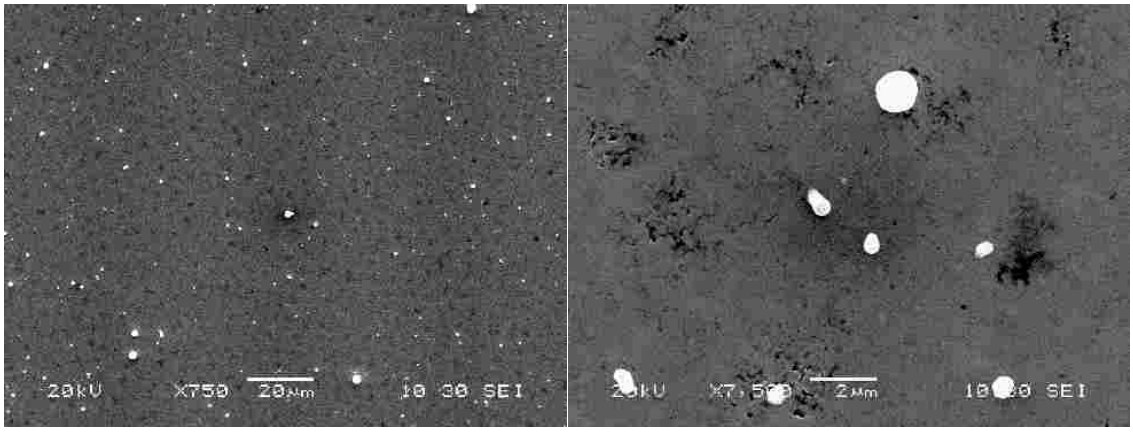

Fig. 5.3. Additional SEM images at magnifications of 750x and 7,500x.

EDS was conducted to determine the elemental composition of these surface features. Fig. 5.4 shows the EDS results for a dark spot located on sample Al-1 with the corresponding SEM image. The detector picked up germanium located around the dark spot with minimal amounts located in the dark spot, indicating a depletion zone. Increased amounts of aluminum were detected in the dark spots. The increase in the silicon intensity confirms these dark spots to be a depletion region, since the EDS electron beam would travel further into the sample if there was a lower depth in the layer. These germanium depletion zones, or diffusion paths, often occur in metal induced crystallization and can range in size from several hundred nanometers to a few micrometers [18]. These depletion regions show the initial steps in the layer transfer process.

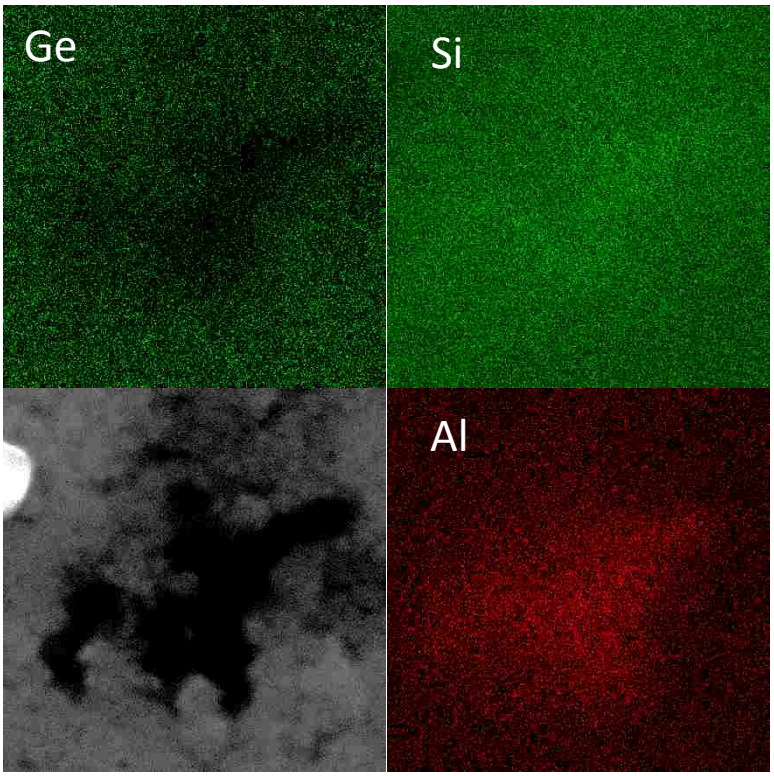

Fig. 5.4 EDS results for a dark spot on Sample Al-1 with corresponding SEM.

EDS was also conducted for a circular hillock located on the surface. The results are seen in Fig. 5.5 with the corresponding SEM image. Germanium is evenly spread throughout the sample. There is an increase in aluminum intensity primarily where the hillock is located. The silicon intensity shows a depletion where the hillock is located indicating and confirming the white spot is raised above the surface, since the electron beam of the EDS detector can only travel so far and is not detecting as much of the silicon layer where the hillock is located, because the hillock is absorbing more of the signal. The formation of Al hillocks from the diffusion of Al through the Ge layer occurs in order to relieve stress on the system [18]. These hillocks represent an additional step in the layer transfer process.

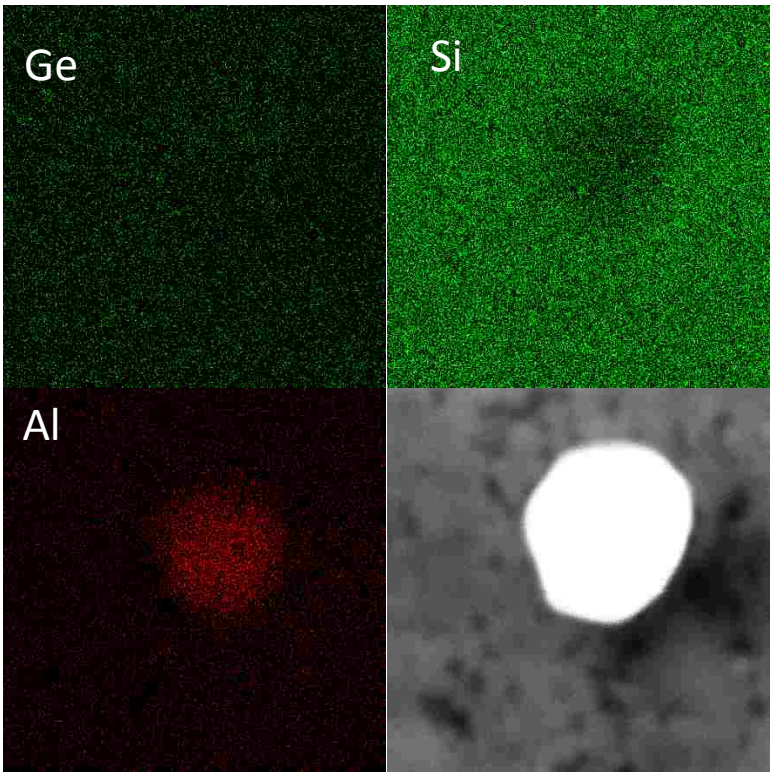

Fig. 5.5. EDS results of light spot located above the surface with SEM image.

Cross-sectional SEM was conducted on this sample to gain more information on the layer transfer process. The results are seen in Fig. 5.6. EDS was attempted on the cross-sectional SEM image of sample Al-1, but was unable to be completed because of the limitations associated with the machine in terms of drifting due to the electron beam accelerating voltage and the high magnification. The cross-section SEM shows the layers with corresponding labels for Sample Al-1. A complete layer transfer has not occurred as seen with the cross-sectional SEM image that shows a small aluminum layer still present between the germanium and SiO_2 layers.

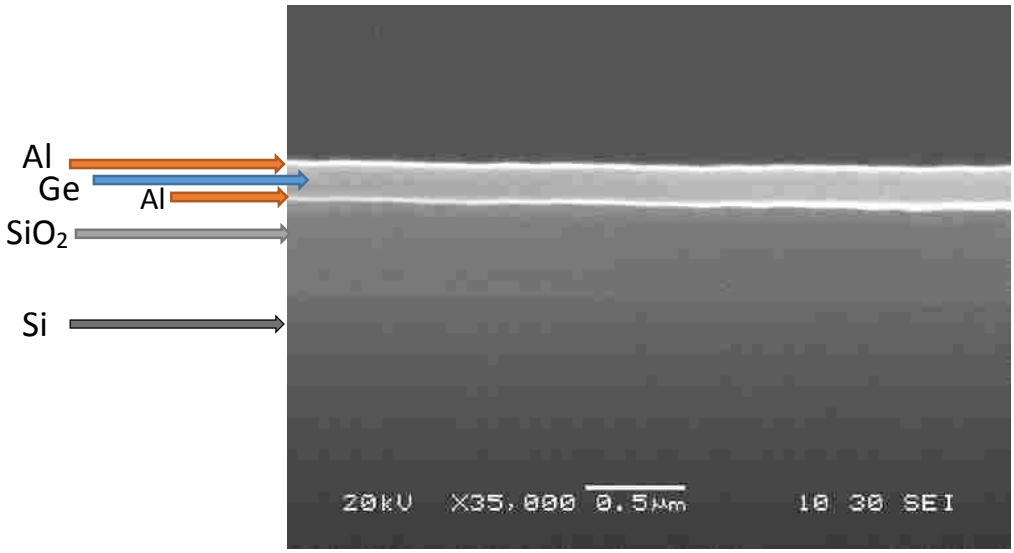

Fig. 5.6. Cross-sectional SEM of sample Al-1.

5.2 SAMPLE AL-2 RESULTS AND DISCUSSION

Sample Al-2 had a 50nm aluminum thickness, 600nm germanium thickness, 480° C set point temperature, and a ramp rate of 1°/sec. SEM results of Sample Al-2 surface are seen in Fig. 5.7. Large craters with a size of approximately 150µm, were found on the surface of this sample. It appears that part of the sample has peeled off due to delamination. Around the crater, there appears to be some small surface features of irregular size. These features are not the same as the ones seen in Al-1. These features could be due to the increase in stress caused by the thicker Ge layer during the annealing process resulting in peeling.

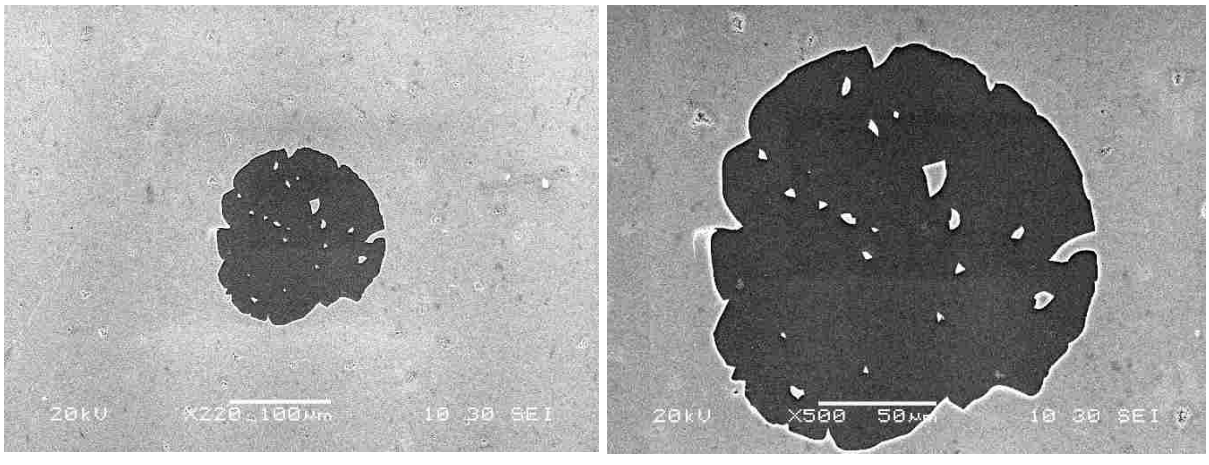

Fig. 5. 7. SEM of a crater on Sample Al-2 surface.

Cross-sectional SEM was also conducted on this sample and the images are seen in Fig. 5.8. As seen with sample Al-1, it appears that not all of the aluminum has diffused through the germanium and layer transfer has not occurred. The increase in the germanium layer as compared to sample Al-1 is also seen in the cross-sectional SEM image.

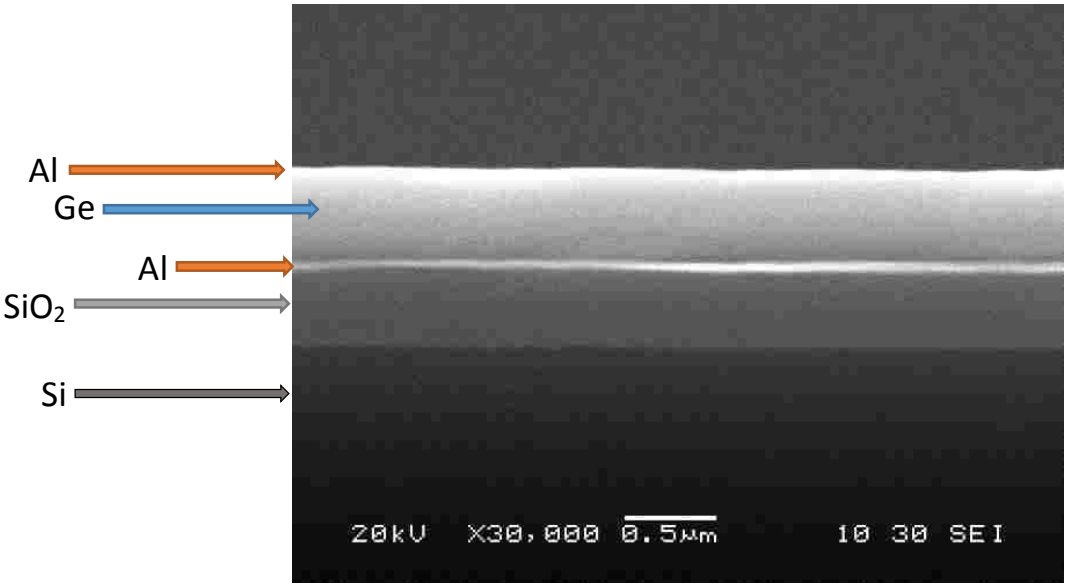

Fig. 5.8. Cross-sectional SEM of sample Al-2.

5.3 SAMPLE AL-3 RESULTS AND DISCUSSION

Sample Al-3 had layer thicknesses of 50nm aluminum and 400nm germanium with a 480° C set point temperature and a ramp rate of 1°/sec. SEM results are seen in Fig. 5.9. This sample had a similar surface morphology as sample Al-1, but this sample appears to have less white spots and more dark spots than Al-1. Fig. 5.9 (a) shows the clustering of light spots and the evenly distributed dark spots. The number of dark spots appears to outnumber the white spots. Fig. 5.9 (b) shows the dark spots appear to be depletion or separation on the surface. Fig. 5.9 (c) shows the white spots or hillocks, on the surface that have a spherical and oval shape and range in size, but can be as large as 2µm. This image also shows the cluster of hillocks, which was similar to sample Al-1. Fig. 5.9 (d) shows a zoomed in image of a dark spot, which appears to be a separation of the surface. These features significantly covered the surface of the sample. No

crystalline features were seen on this sample. Despite the difference in temperature and a thicker germanium layer, the surface features were similar to sample Al-1. The increase in dark spots and decrease in hillocks could be attributed to the increase in germanium thickness, because the aluminum has a thicker distance to transfer through, slowing the layer transfer process.

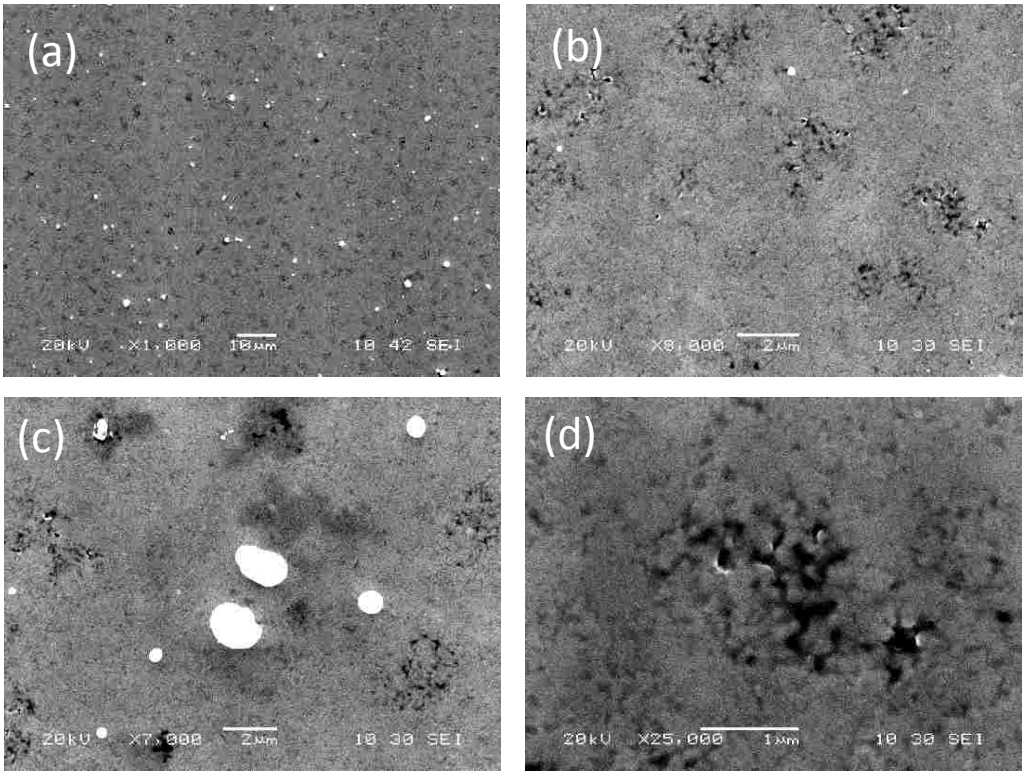

Fig. 5.9. SEM images for Sample Al-3, (a) magnification 1,000x, (b) dark spots, (c) light spots, (d) zoomed in dark spot.

5.4 SAMPLE AL-4 RESULTS AND DISCUSSION

Sample Al-4 had thickness of 50nm and 200nm for aluminum and germanium, respectively. The set point temperature was 500°C and the ramp rate was 0.1 °C/s. An increase in temperature was used to promote crystalline growth. A lower ramp rate was chosen to decrease stress on the sample during the layer transfer process. SEM was conducted on this sample to investigate the surface features. The SEM results are seen in Fig. 5.10 showing delamination or cloud-like

features on the surface. Fig. 5.10 (a) shows a zoomed out version of the sample and how these features appear to cluster together and were seen throughout the sample surface. Fig. 5.10 (b) shows the irregular shape of these features on the surface. There were also cracks seen throughout the surface and can be seen in Fig. 5.10 (c) and (d) indicating an increase in stress on the surface, in addition to a zoomed in version of the features showing the holes and gaps in the features' structure. The features appear around the cracks, as well as in open space. These features do not appear to have any crystalline structure and appear to be peeling off the surface. In addition, there does not appear to be any crystalline features present on the surface. The delamination features appear to be raised on the surface. There is some differences in the surface textures seen in Fig. 5.9 (d) next to the delamination features. Sample Al-4 has a much different appearance than sample Al-1, Al-2, and Al-3.

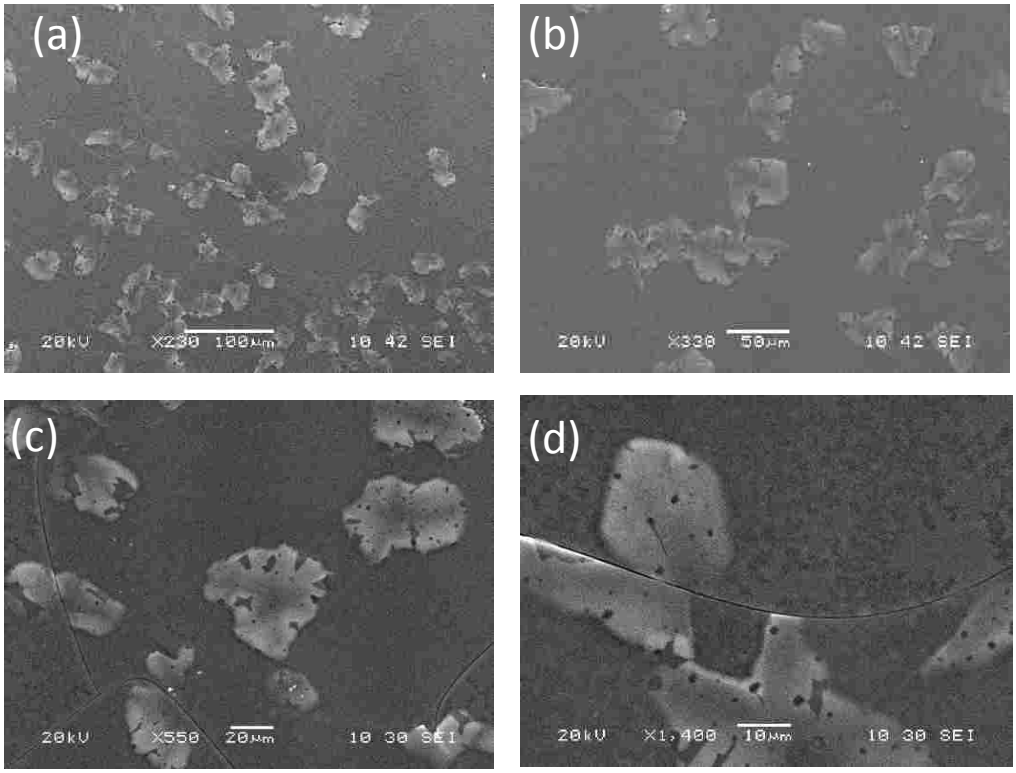

Fig. 5.10. SEM of the surface features on Sample Al-4.

EDS was conducted to determine the elemental composition of these features. In Fig. 5. 11, the blue box on the right image in Fig. 5.11 shows the SEM spot used for EDS analysis. This

spot was chosen because of the delamination feature and the crack present, in addition to the differences in surface texture located to the right of the white spot with holes. Also, the right image in the bottom left corner appears to have surface coverage present.

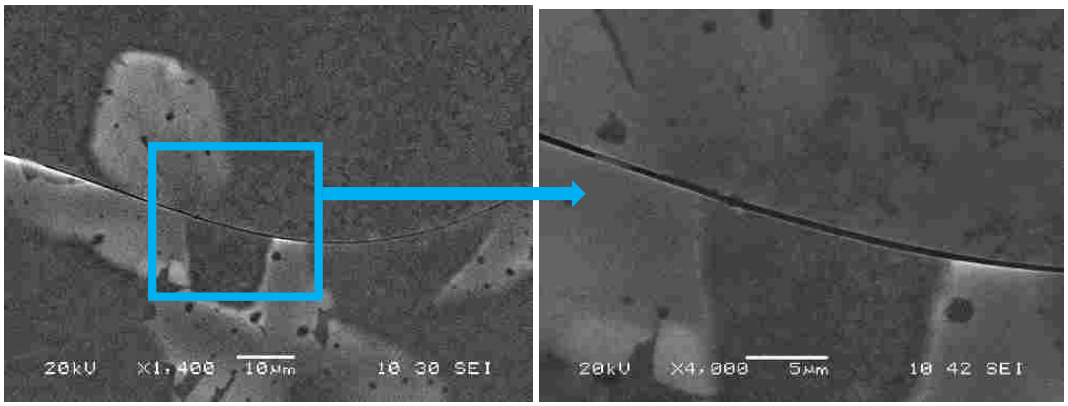

Fig. 5. 11. Right: SEM used for EDS analysis and Left: SEM showing where the zoomed feature is located.

EDS mapping results for Sample Al-4 are seen in Fig. 5.12 with the corresponding SEM image. Al, Ge. Si, O, and C were detected on the sample. The delamination spots with holes have a higher concentration of germanium and appear to be raised above the surface since the Si signal is weaker in those spots indicating the signal is being absorbed, limiting how far the EDS electron beam reaches. The delamination spots appear to be germanium peeling off of the surface, as indicated in the bottom left of the corresponding SEM image. The Al intensity is increased where the germanium is peeling off from the surface. There is a depletion of germanium where the dark regions are located. Aside from increase in aluminum intensity in the lower left corner, the Aluminum is evenly dispersed throughout the sample.

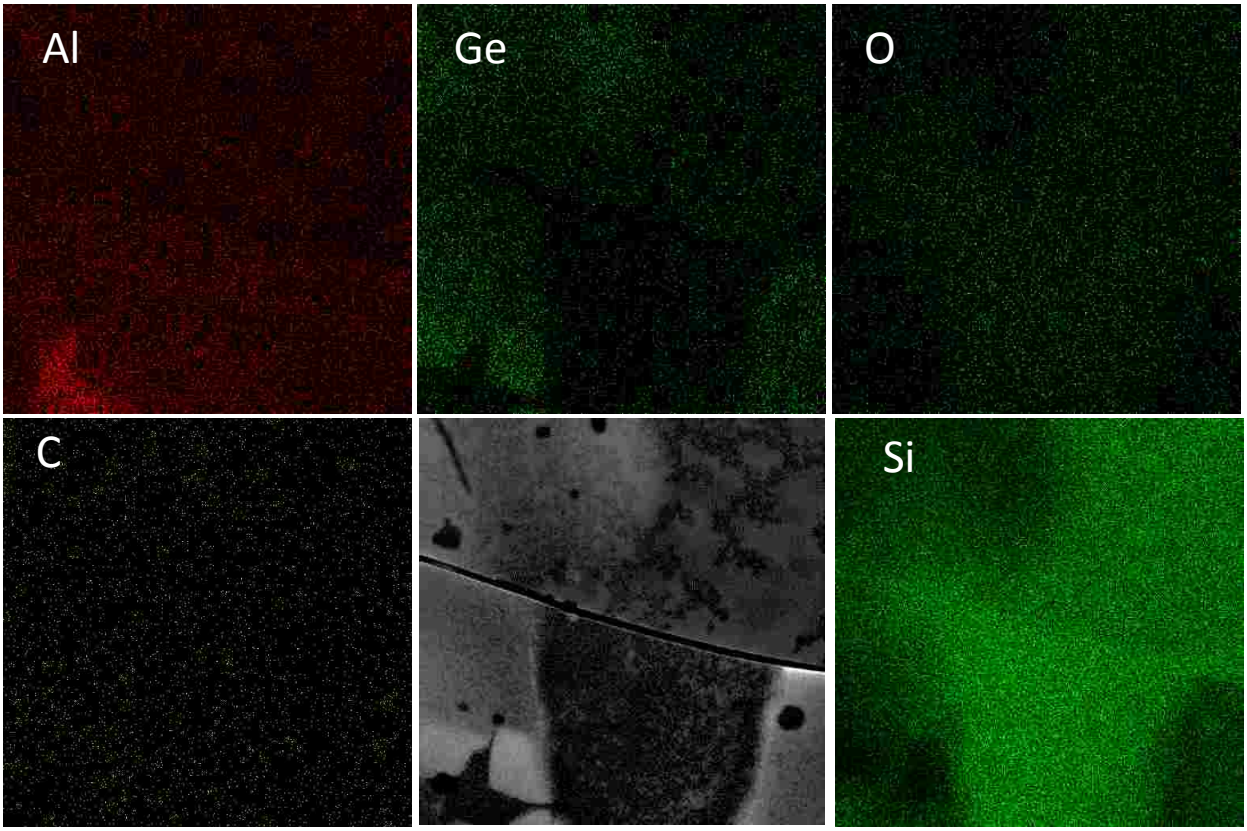

Fig. 5.12. EDS results for Sample Al-4 with corresponding SEM.

EDS "Point and shoot" was also conducted on sample Al-4 to determine more specifically the elemental composition of specific spots on the sample. Four points were analyzed and the results are seen in Fig. 5.13 with the corresponding SEM and point locations. Point 1 was taken where the crack in the sample was located, and points 2-4 were located on either side of the split. Table 5.2 shows the atomic percentage for each point. The EDS results for Point 1 indicates that the crack in the sample contains minimal amounts of germanium and aluminum and is mostly composed of silicon, which is confirmed by looking at the EDS mapping of Sample Al-4 in Fig. 5.12. Point 2 and 3 were located on a light region and the results show an increase in germanium intensity, which confirms the EDS mapping results that the light spots contain a higher germanium amount. Point 4 was located on a darker region and the EDS spectrum indicates that this location is depleted in germanium.

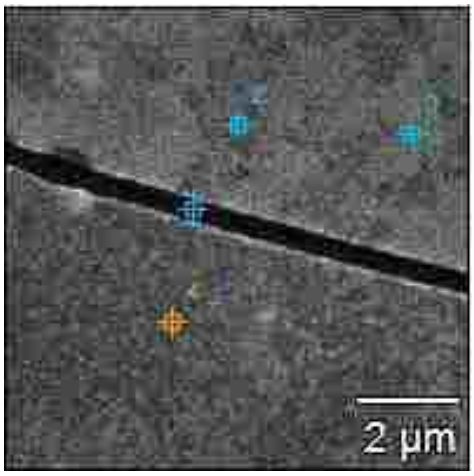

Fig. 5.13. EDS point and shoot of Sample Al-4 with the corresponding SEM including the point locations analyzed.

Table 5.2 Atom Percentages for Specific Location of EDS for Sample Al-4

Point #	Carbon	Aluminum	Silicon	Germanium
1	52.93	0.53	45.24	0.52
2	55.31	2.29	35.02	3.81
3	49.99	2.30	39.55	4.60
4	49.44	2.94	41.16	1.87

5.5 SAMPLE AL-5 RESULTS AND DISCUSSION

Sample Al-5 had a germanium thickness of 600nm, a set point temperature of 500℃ and a ramp rate of 0.1℃/s. SEM results for sample Al-5 are seen in Fig. 5.14. The upper left image shows cracks found on the surface. The bottom left and right images in Fig. 5.14 show a zoomed in image of the cracks. EDS mapping was conducted on this feature in addition to the dark region located by the crack. The bottom left shows a darks spot, which appears to be a depletion area. The upper right SEM image in Fig. 5.14 shows a mostly uniform surface with an interesting feature where the orange arrow is pointed to, and appears to be raised above the surface. This sample had similar features in terms of the cracks present as sample Al-4, which could be attributed to the ramp rate and growth temperature.

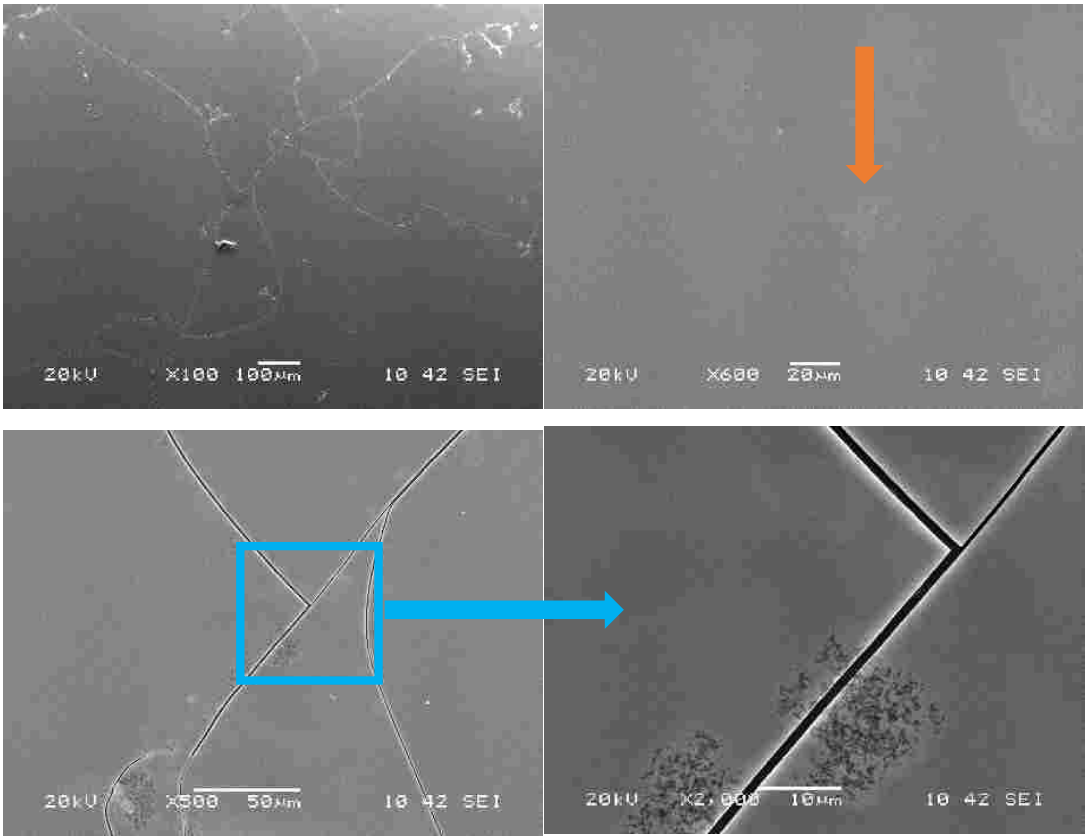

Fig. 5.14. SEM results of Sample Al-5 showing cracks on the surface.

Fig. 5.15 shows the EDS Mapping results for Sample Al-5 on the split in the surface with the dark region surrounding it. Aluminum intensity is significantly higher where the dark region is located, indicating this is a depletion region, since there is also a lack of germanium is this area. This feature is similar to Al-1 and Al-3 dark regions. The germanium intensity is strong due to the increase in the thickness of this layer. The crack in the surface appears to be depleted of both aluminum and germanium and seems to be composed of silicon and oxygen, (SiO_2). Carbon was detected, but is mostly evenly spread out along the surface, except for the crack. This is could be an artifact of organic contamination with utilizing SEM and EDS at higher magnifications.

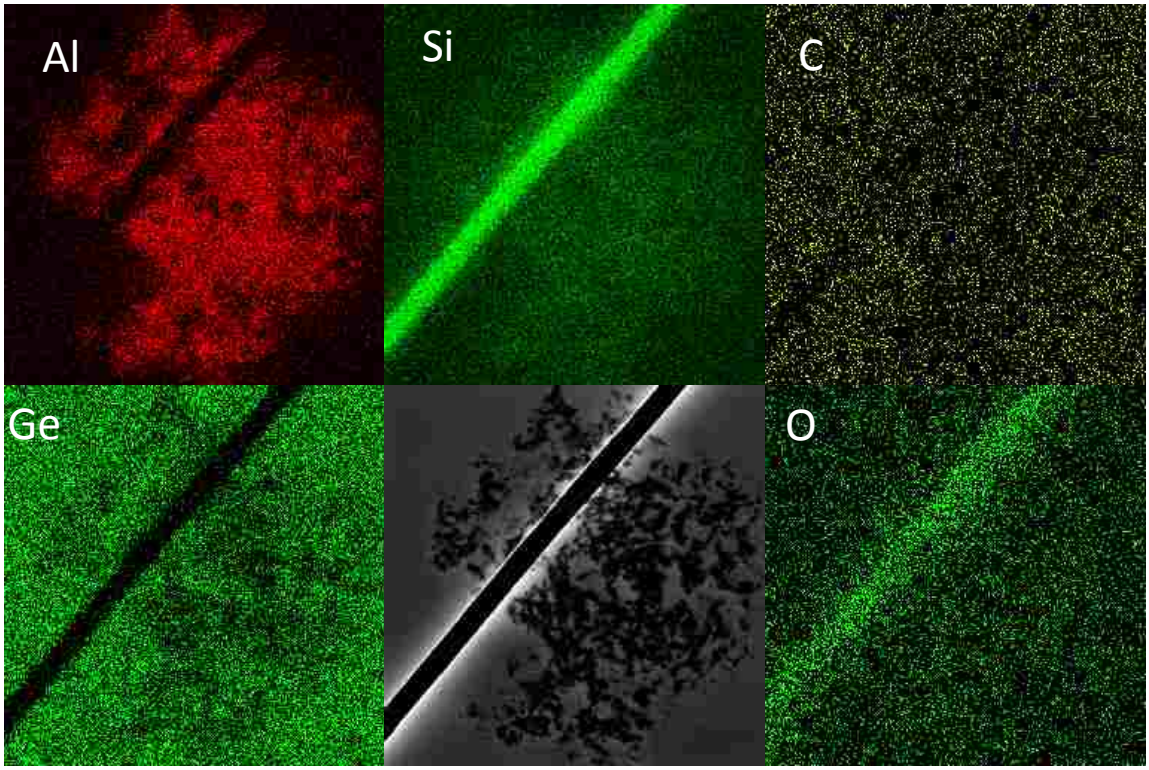

Fig. 5.15. EDS Results for Sample Al-5 for the crack and dark region located on the surface.

EDS mapping was also conducted on the raised feature on the surface and the results are seen in Fig. 5.16. The intensity for germanium and aluminum appear to be the same throughout this region. There does not appear to be any difference with intensity for this surface feature. This feature could be the beginning of the delamination process that occurs from an increase in stress on the sample.

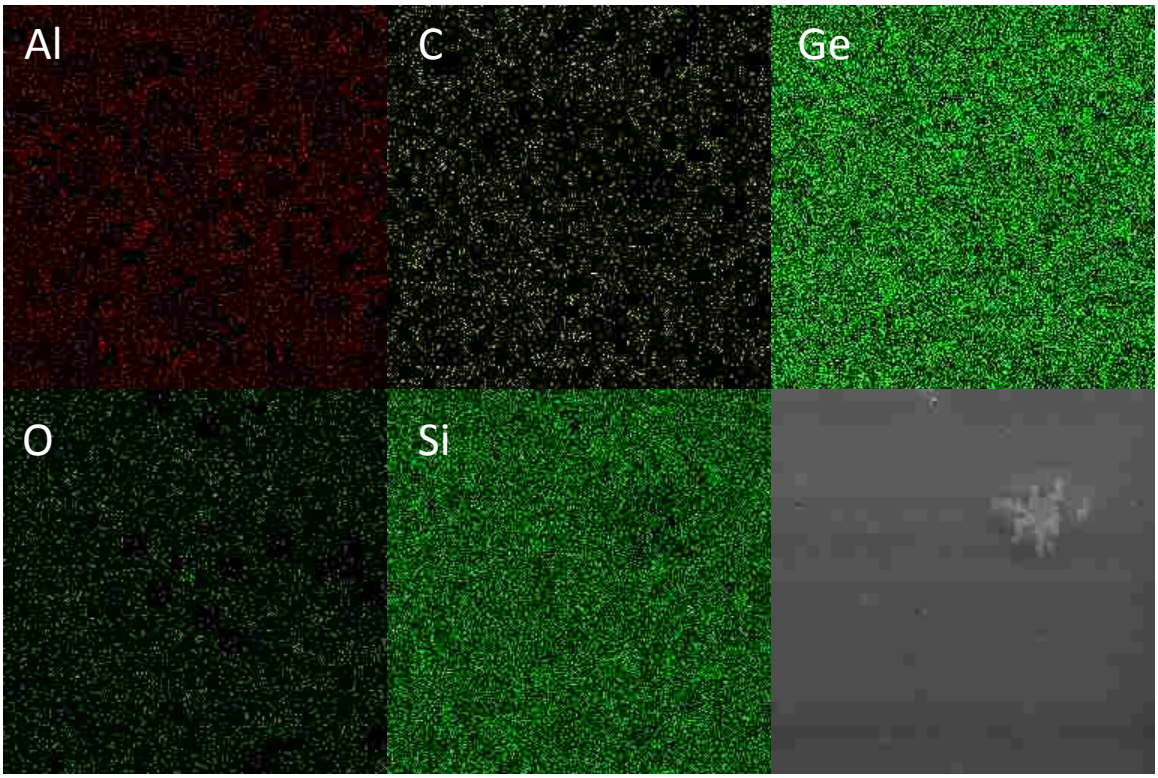

Fig. 5.16. EDS results for Sample Al-5 for the interesting raised feature located on the surface.

Additional surface features were found on Sample Al-5 and can be seen in Fig. 17. The upper left shows a crater feature that results from delamination down to the substrate, similar to the one seen in sample Al-2, except this feature is only approximately 30μm in diameter and is irregular in shape. This image also shows an increase in dark depletion regions surrounding the crater. The upper right and lower right SEM images in Fig. 5.17 show more delamination features ranging in size from approximately 50μm to 150μm. The bottom right image shows a small depletion region in the upper left corner. The lower left SEM image shows the irregular distribution of these features located on the surface of Sample Al-5. This sample had a wide varied of surface features that ranged in size and shape. EDS "Point and Shoot" was conducted on the oval features to gain more insight on the elemental composition of these aspects.

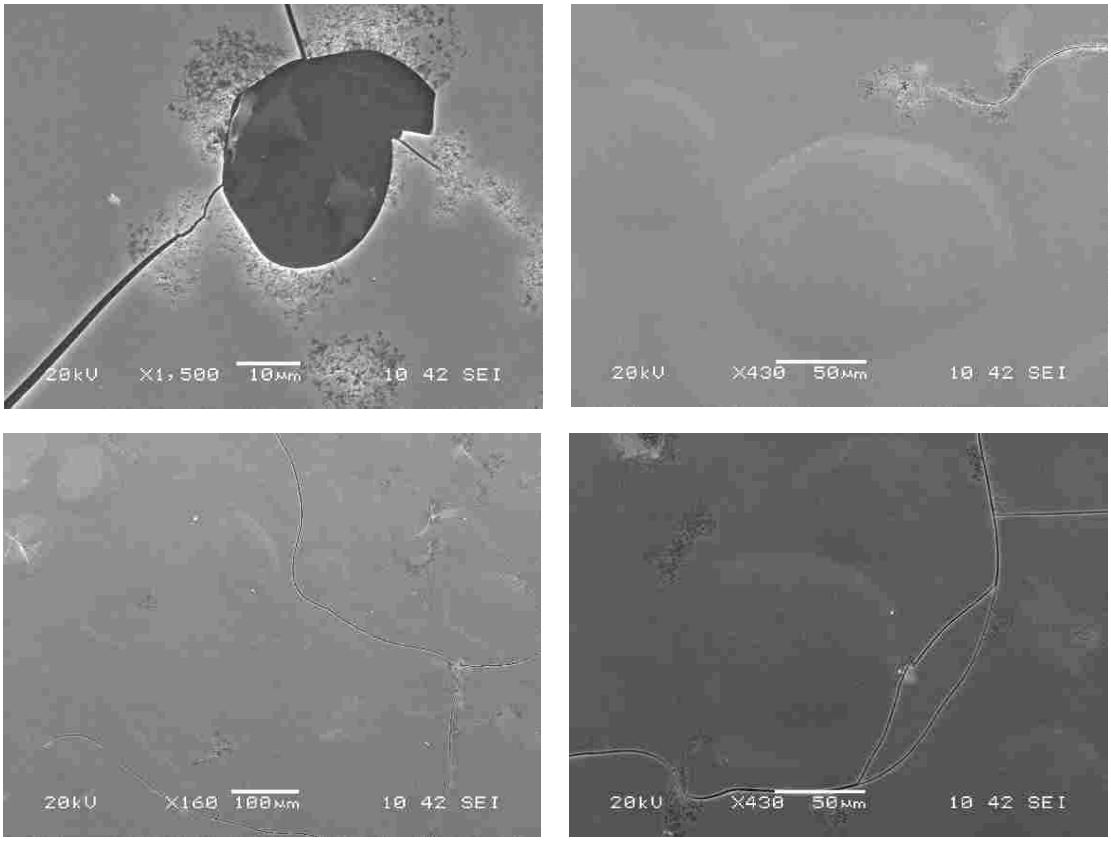

Fig. 5.17. Additional SEM results of surface features found on Sample Al-5.

EDS specific point measurement results for the raised delamination feature and three additional points surrounding this feature, including one on the depletion region, open space, and the crack, are seen in Fig. 5.18. The atom percentages are seen in table 5.3. Point 1, 2 and 4 had large intensities of germanium. Point 3 did have a stronger intensity of aluminum as compared to the other points, which indicts and confirms that those dark regions are depletion zones for germanium and have an increase in aluminum. The raised feature, point 1, did not differ significantly from point 4 in terms of atom percentages for germanium, silicon, and aluminum. This features could be the start of delamination of the germanium, which eventually leads to peeling, resulting in delamination down to the surface as seen in Fig. 5.17 upper left.

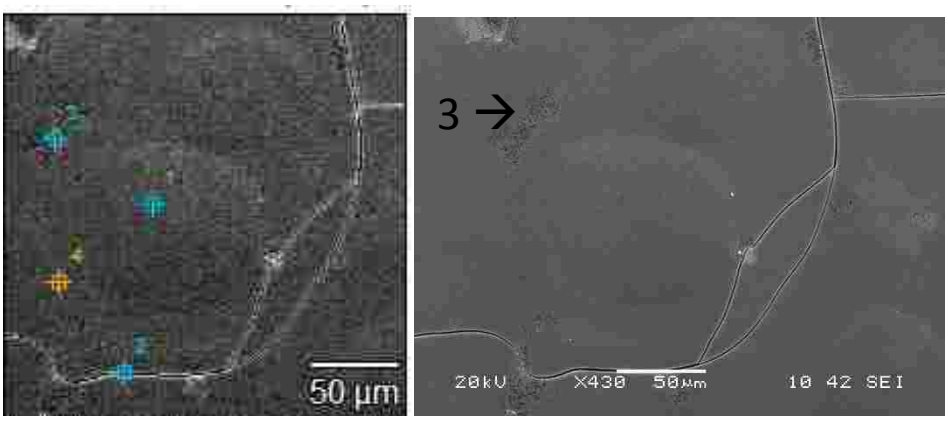

Fig. 5.18. EDS Point and Shoot on the additional surface features found on Sample Al-5.

Table 5.3 Atom Percentages for Specific Point Measurement for Sample Al-5

Point #	Carbon	Aluminum	Silicon	Germanium
1	37.15	1.13	24.88	34.99
2	27.28		25.15	34.95
3	19.38	16.61	28.15	10.93
4	38.87		25.66	35.47

5.6 Comparison and Conclusions of Characterization Study of the AIC-Ge Process

Complete layer transfer did not occur in any of the samples, which was observed in the SEM cross-section analysis. The effects of the AIC process were observed in this study. Samples Al-1 and Al-3 had similar surface features that consisted of hillocks and depletion regions, both of which were rich in aluminum. The increase in germanium thickness of sample Al-2 could have contributed to the large delamination features seen on the surface. The temperature was increased to promote crystalline growth. The ramp rate was lowered to decrease stress on the sample during the layer transfer process. However, with sample Al-4, significant delamination was seen on the surface, more specifically germanium was peeling off of the surface. In addition, cracks were observed on both sample Al-4 and Al-5 indicating stress had occurred. Sample Al-5 had delamination down to the substrate present and raised-oval features, which could be the beginning of the delamination process. Delamination down to the substrate was observed for samples Al-2 and Al-5, which both had a germanium thickness of 600nm. Ultimately, a thicker

germanium layer is preferred, but increases stress on the sample. With larger temperatures, it is more likely stress will occur. Additionally, an insufficient aluminum layer could have contributed to the stress seen in each of the samples. The increase in germanium thickness magnified the delamination. Decreasing the stress on the sample during the layer transfer process is necessary in achieving a more uniform high quality surface without cracks or delamination.

CHAPTER 6

CONCLUSIONS

6.1 Summary

Silicon currently dominates the solar cell industry due to its abundant availability and cheaper costs, but is limited when it comes to efficiencies and absorption. III-V solar cells have pioneered the solar cell field in terms of efficiency and multijunction applications, reaching efficiencies greater than 45%. However, III-Vs are limited to specialty applications, such as space, because of their high cost due to the growth techniques, scarcity of materials, and substrate costs. The substrate cost makes up the majority of the III-V solar cell cost, making it difficult to compete with silicon solar cells. Polycrystalline material can be difficult to work with and there is still a long way to go in making III-V's incorporated into terrestrial applications. At ODU, there was access to limited characterization tools, which were used in this research. There are more characterization techniques that can expand upon the ones used in this study. This thesis investigated two growth processes for achieving cheaper substrates to reduce the costs associated with III-V materials.

The first process was directly growing InP and InAs on cheaper substrates, Mo foils, by MOCVD. A growth time study was conducted with the direct growth of InP on Mo foils and showed Volmer Weber growth that with an increase in growth time did improve surface coverage and coalescing of islands, especially from doubling the growth time from 49 min to 98 min. Volmer Weber growth occurred because of the lattice mismatch between the Mo foil and InP. Sample P-1 did have arsenic contamination, but samples P-2 and P-3 were grown successfully without contamination. Sample P-2, growth time of 98 minutes, had slightly better surface coverage than Sample P-3 and aligned better with the PL of an InP substrate. Although a complete continuous medium was not achieved with the 147 minutes of growth time, the results did show promising steps towards polycrystalline InP on metal foils with lattice constants and bandgaps that were very similar to the accepted values of InP. Typically, larger grain sizes are seen at higher temperatures larger than 545°C, but the temperature may need to be lower to achieve a continuous film.

InAs is extremely useful in optoelectronic devices requiring long-wavelengths and solar cell industry with its low bandgap and high electron mobility. However, substrate costs are very high for InAs due to growth process and scarcity of materials. The direct growth of InAs on Mo foil was also conducted in order to take steps toward low-cost polycrystalline substrates. One sample was grown with a growth time of 49 minutes and showed that it is possible to apply the direct growth process with indium and arsenic on molybdenum foils. Polycrystalline material was formed and despite islanding that was present, the lattice constant and bandgap of this sample aligned very closely with the accepted values for InAs. Surface roughness and coverage was also conducted that indicated 3-D islanding consistent with Volmer Weber growth and a coverage of approximately 55%. This process showed that directly growing polycrystalline InAs on a cheaper substrate, Mo foils, is possible.

Germanium is an important substrate for III-V applications and is often used as the bottom cell for multijunction III-V solar cells because of its lower bandgap and lattice match capabilities, but is still expensive when compared to silicon. The second process involved the aluminum induced crystallization of germanium by layer transfer in order to decrease the costs associated with typical Ge substrates. A characterization study was conducted for varying set point temperatures ranging from 480 °C to 500°C, ramp rates from 1°C/s to 0.1°C/s, and germanium layer thickness from 200nm to 600nm. The results showed the effects of the growth process on the germanium and aluminum layer transfer, which included cracking and significant depletion regions. Samples Al-1 and Al-3 had the same ramp rate, but different Ge layer thicknesses and set point temperatures. These two samples had very similar surface features, including depletion regions and hillocks seen throughout the sample. The slight difference was Al-1 had more hillocks, which could be from the thinner Ge layer, allowing more Al to diffuse through. Samples Al-4 and Al-5 had a ramp rate of 0.1°C/s and had very different surface features than the other three samples. These samples had cracks and small craters seen throughout the sample, indicating an increase in stress on the sample. They did have depletion regions and with EDS Mapping it was confirmed that this large depletion regions were in fact germanium depleted, and rich in aluminum. The hillocks in the other samples were also confirmed to be made of aluminum. Samples Al-2 and Al-5 both had a germanium thickness of 600nm and delamination down to the surface present, which could be attributed to the thicker germanium layer intensifying the stress on the system. Despite varied ramp rates, setpoint

temperatures, and germanium thicknesses, each sample had some form of stress present, which could have resulted from the insufficient aluminum thickness.

High substrate costs for III-V solar cells have limited applications to space or high concentration systems. However, their high efficiency and optimal qualities make them ideal for expanding III-Vs to terrestrial applications and could vastly improve how much clean energy is produced from the solar industry if the costs were lowered. These two process show promising steps towards developing cheaper substrates for III-Vs. Although Ge is not a III-V material, it is very important for III-V multijunction applications, especially with GaAs. Aluminum induced crystallization of germanium could provide a cheaper way of creating low-cost, but high quality Ge substrates. InP and InAs are also very expensive substrates, but if costs associated with these materials were decrease, the use of these materials could be vastly expanded. Using alternative substrates to grow on, such as metal foils, provides a cheaper method for polycrystalline III-V material. Improving the efficiency of terrestrial applications by expanding III-V solar cells is important in making a bigger impact on lessening the world's dependency on fossil fuel.

6.2 Future Works

This work can be expanded upon in the efforts towards achieving low-cost, high-quality polycrystalline substrates. Next steps include taking continued steps towards a continuous film by adding a surfactant to alter the surface energy or decreasing the growth temperature. Additional parameters, such as the V/III ratio can also be altered and investigated. Another key aspect, would be to investigate surface details that could affect island growth. Additionally, the growth time study can be completed for InAs on Mo, and the direct growth process can be expanded to additional III-V binaries. When a continuous medium is achieved, a ternary can be fabricated, InPAs, to directly grow on metal foils to create a virtual substrate that can be engineered to a specific lattice constant. Lastly, when a continuous film is achieved, a multijunction solar cell structure can then be built upon the substrates that were directly grown on Mo foil in order to reduce the costs associated with typical substrate costs.

REFERENCES

[1] H. Cotal, C. Fetzer, J. Boisvert, G. Kinsey, R. King, P. Hebert, *et al.*, "III-V multijunction solar cells for concentrating photovoltaics," *Energy and Environmental science,* vol. 2, pp. 174-192, 2008.

[2] P. A. Lynn, *Electricity from Sunlight: An introduction to Photovoltaics*. United Kingdom: John Wiley & Sons, 2010.

[3] G. Knier. (2008, March 8). *How do Photovoltaics Work?* Available: https://science.nasa.gov/science-news/science-at-nasa/2002/solarcells

[4] J. P. Connolly, D. Mencaraglia, C. Renard, and D. Bouchier, "Designing III-V multijunction solar cells on silicon," *Progress in Photovoltaics: Research and Applications,* vol. 22, pp. 810-820, 2013.

[5] N. E. Sosa, T. G. v. Kessel, Y. Martin, and H. J. Hovel, "III-V Photovoltaics- Recent Developments and Prospects," *ECS Transactions,* vol. 33, pp. 923-925, 2010.

[6] M. Zheng, Z. Yu, T. J. Seok, Y.-Z. Chen, R. Kapadia, K. Takei, *et al.*, "High optical quality polycrystalline indium phosphide grown on metal substrates by metalorganic chemical vapor deposition," *Journal of Applied Physics,* vol. 111, 2012.

[7] D. Decoster and J. Harari, *Optoelectronic Sensors*. Hoboken, NJ: John Wiley & Sons, Inc., 2009.

[8] A. G. Milnes and A. Y. Polyakov, "Indium arsenide: a semiconductor for high speed and electro-optical devices," *Material Science and Engineering* vol. B18, pp. 237-259, 1993.

[9] (March 20, 2017). *Electrical Properties Si-Silicon*. Available: http://www.ioffe.ru/SVA/NSM/Semicond/Si/electric.html#Surface

[10] D. Kiriya, M. Zheng, R. Kapadia, J. Zhang, M. Hettick, Z. Yu, *et al.*, "Morphological and spatial control of InP growth using closed-space sublimination," *American Institute of Physics,* vol. 112, 2012.

[11] J. S. Ward, T. Remo, K. Horowitz, M. Woodhouse, B. Sopori, K. VanSant, *et al.*, "Techno-economic analysis of three different substrate removal and reuse strategies for III-V solar cells," *Progress in Photovoltaics,* vol. 24, pp. 1284-1292, 2016.

[12] I. Vurgaftman, J. Meyer, and L. Ram-Mohan, "Band Parameters for III-V compound semiconductors and their alloys," *Journal of Applied Physics,* vol. 89, 2001.

[13] T. R. Merritt, M. A. Meeker, B. A. Magill, G. A. Khodaparast, S. McGill, J. G. Tischler, *et al.*, "Photoluminescence lineshape and dynamics of localized excitonic transitions in InAsP epitaxial layers," *Journal of Applied Physics,* vol. 115, 2014.

[14] E. L. McClure, M. A. Slocum, R. K. Hailstone, P. T. Furrey, Z. S. Brittner, S. Maximenko, *et al.*, "In-Situ Stress Analysis for Aluminum-Induced Crystallization of Germanium as a Function of Anneal Ramp Time," presented at the Photovoltaic Specialists Conference, Portland, Oregon, 2016.

[15] Available: http://www.mtixtl.com/

[16] G. B. Stringfellow, *Organometallic Vapor-Phase Epitaxy: Theory and Practice*, Second ed. London, UK: Academic Press, 1999.

[17] M. Razeghi, *The MOCVD Challenge: A survey of GaInAsP-InP and GaInAsP-GaAs for photonic and electronic device applications*, Second ed. Boca Raton, Fl: CRC Press, 2011.

[18] T. Zhang, Y. Huang, W. Zhang, F. Ma, and K. Xu, "Effect of stacking sequence on crystallization in Al/a-Ge bilayer thin films," *Journal of Vacuum Science Technology*, vol. 32, 2014.

[19] K. Nakazawa, K. Toko, N. Saitoh, N. Yoshizawa, N. Usami, and T. Suemasu, "Effect of Ge/Al thickness on Al-induced crystallization of amorphous Ge layers on glass substrates," *Physics Status Solidi*, vol. 10, pp. 1781-1784, 2013.

[20] J.-Y. Lin and P.-Y. Chang, "Growth of poly-crystalline silicon-germanium on silicon by aluminum-induced crystallization," *Thin Solid Films,* pp. 6893-6899, 2012.

[21] B. D. Cullity and S. R. Stock, *Elements of X-Ray Diffraction*, Third ed. Upper Saddle River, New Jersey: Prentice-Hall, Inc., 2001.

[22] M. A. Reshchikov, "Temperature dependence of defect-related photoluminescence in III-V and II-VI semiconductors," *Journal of Applied Physics,* vol. 115, 2014.

[23] M. Matsuoka, M. Saito, and M. Anpo, "Photoluminescence Spectroscopy," in *Charaterization of Solid Materials and Heterogeneous Catalysts: From Structure to Surface Reactivity*. vol. 1&2, M. Che and J. C. Vedrine, Eds., ed Weinheim, Germany: Wiley-VCH, 2012, pp. 149-153.

[24] Y. Wang and V. Petrova, "Scanning Electron Microscopy," in *Nanotechnology Research Methods for Foods and Bioproducts*, G. W. Padua and Q. Wang, Eds., ed Oxford, Uk: Wiley-Blackwell, 2012, pp. 103-126.

[25] G. Friedbacher, "Atomic Force Microscopy (AFM)," in *Surface and Thin Film Analysis: A Compendium of Principles, Instrumentation, and Applications*, G. Friedbacher and H. Bubert, Eds., Second ed Weinheim, Germany: Wiley-VCH, 2011, pp. 443-464.

[26] I. V. Grishagin, "Automatic cell counting with ImageJ," *Analytical Biochemistry*, vol. 473, pp. 63-65, 2015.

[27] V. Prathibha, S. Karthika, J. Cyriac, C. Sudarasanakumar, and N. V. Unnikrishnan, "Synthesis of pure anatase TiO_2 nanocrystals in SiO_2 host and the determination of crystal planes by ImageJ," *Materials Letters*, vol. 65, pp. 664-666, 2011.

[28] R. Kapadia, Z. Yu, H.-H. H. Wang, M. Zheng, C. Battaglia, M. Hettick, *et al.*, "A direct thin-film path towards low-cost large-area III-V photovoltaics," *Scientific Reports*, vol. 3, 2013.

[29] W. Wei, X.-Y. Bao, C. Soci, Y. Ding, Z.-L. Wang, and D. Wang, "Direct Heteroepitaxy of Vertical InAs Nanowires on Si Substrates for Braod Band Photovoltaics and Photodetection," *Nano Letters*, vol. 9, pp. 2926-2934, 2009.

[30] J. A. Venables, *Introduction to Surface and Thin Film Processes*. Cambridge: Cambridge University Press, 2003.

[31] G. Abadias, L. Simonot, J. J. Colin, A. Michel, S. Camelio, and D. Babonneau, "Volmer-Weber growth stages of polycrystalline metal films probed by in situ and real-time optical diagnostics," *Applied Physics Letters*, vol. 107, 2015.

[32] H. Z. Yu and C. V. Thompson, "Grain growth and complex stress evolution during Volmer-Weber growth of polycrystalline thin films," *Aeta Materialia*, vol. 67, 2014.

[33] W. Shafer, "PDF Card No.: 00-010-0216," Journal of Physical Chemistry1957.

[34] H. K. Choi, "Mid-infrared lasers fabricated from III-V compound semiconductors " *Current Opinion in Solid State and Materials Science*, vol. 1, pp. 212-217, 1996.

[35] Z. Yin and X. Tang, "A review of energy bandgap engineering in III-V semiconductor alloys for mid-infrared laser applications," *Solid-State Electronics*, pp. 6-15, 2007.

[36] S. Mokkapati and C. Jagadish, "III-V compound SC for optoelectronic devices," *Materials Today*, vol. 12, 2009.

[37] S. Pal, S. D. Singh, V. K. Dixit, T. K. Sharma, R. Kumar, A. K. Sinha, *et al.*, "Crystalline and band alignment properties of InAs/Ge (111) heterostructure," *Journal of Alloys and Compounds,* pp. 393-398, 2015.

[38] I. A. Gazz, "PDF Card No.: 01-073-1984," *Chim. Ital.,* vol. 70, 1940.

[39] R. Contreras-Guerrero, S. Wang, M. Edirisooriya, W. Priyantha, J. S. Rojas-Ramirez, K. Bhuwalka, *et al.*, "Growth of heterostructures on InAs for high mobility device applications," *JOurnal of Crystal Growth,* vol. 378, pp. 117-120, 2013.

VITA

Marlene Lichty
Department of Electrical and Computer Engineering
Old Dominion University
Norfolk, VA 23529

EDUCATION:

B.S. Computer Engineering May 2014
Christopher Newport University
Newport News, VA

PUBLICATIONS:

Direct MOCVD Epitaxial Growth of III-V Alloys on Mo for Low Cost PV Applications
Marlene L Lichty, Sean Babcock, Tasnuva Ashrafee, Grace Rajan, Sylvain Marsillac, Seth M Hubbard, Elisabeth L McClure, Christopher G Bailey
43rd IEEE Photovoltaic Specialists Conference, June 2016

Investigation of Direct MOCVD Epitaxial Growth Time of III-V Materials on Metal Foils
Marlene L Lichty, Sean Babcock, Tasnuva Ashrafee, Grace Rajan, Sylvain Marsillac, Seth M Hubbard, Elisabeth L McClure, Christopher G Bailey
44th IEEE Photovoltaic Specialists Conference, June 2017